Multi-wavelength observations of magnetic bright points in the lower solar atmosphere

Masoumeh Izadparast

Thesis submitted for the degree of
Master of Science in Astronomy Master of Science

Institute of Theoretical Astrophysics
University of Oslo

December 2015

Acknowledgements

I wish to express my sincere thanks to Prof. Luc Van der Voort Rouppe, Dr. Shahin Jafarzadeh, and Dr. Pia Zacharias to give me this honor to be my supervisors. Thank you for being so supportive and offering me this project. I would appreciate your help and generosity to take your time for me, helping me to learn new subjects. You were very patient with my questions and difficulties.

I thank J. de la Cruz Rodriguez for providing the 6173 $\mathring{A}$ data. I am also grateful to A. Cristaldi, M. Falco, and S. Criscuoli for SST observations of the 6302 $\mathring{A}$ and Ca II H datasets. The Swedish 1-m Solar Telescope is operated on the island of La Palma by the Institute for Solar Physics of Stockholm University in the Spanish Observatorio del Roque de los Muchachos of the Instituto de Astrof′isica de Canarias.

I would also appreciate my lecturers and faculties in the course of my education at the Institute of theoretical astrophysics. I would like to express my feeling to my friends in the basement. You were very kind and friendly, I would not forget this period of my life in Norway with your company.

I also take this opportunity to thank all my family members for motivating me to go forward, when I was tired and desperate. I would appreciate your support. My special thanks to my parent for your endless love. ...

Table of Contents

Abstract

Magnetic bright points (MBPs) are small-scale (generally kG) magnetic features, ubiquitous in the lower solar atmosphere, and are a manifestation of solar magnetism. They represent the cross-sections of thin flux tubes in different heights. These flux tubes are generated by the advection of magnetic lines from the body of granules into their boundaries in intergranular areas. Due to the convective collapse along magnetic field lines and compression of the bundles, the magnetic field is intensified. The hot and opaque plasma in the deeper layers within the flux tube radiates from the walls, and therefore, a MBP appears bright in the base of photosphere.

In this thesis, we observed MBPs in four different passband filters sampling different heights in the solar atmosphere. Using high-spatial and high-temporal resolution datasets taken with the Solar Swedish Telescope (SST), we study the physical and dynamical properties of MBPs in a quiet sun region close to the solar disk center.

The MBPs were detected using a semi-automated algorithm, which comprises a manual selection and an automated detection algorithm using a scheme of iterative solutions. They were further traced in time-series of images by means of a tracking algorithm. The advantages of applying this method to identify MBPs are to prevent misidentification of MBPs from other non-magnetic bright features. With the help of these algorithms, we extracted physical (such as, size and brightness) and dynamical (such as, horizontal velocity and lifetime) quantities of the identified MBPs. The extracted parameters were analyzed and discussed afterwards.

The analysis of outcomes indicates that the MBPs observed in the lower photosphere live longer and have smaller size on average, while the MBPs residing in the upper photosphere/low chromosphere have found to be brighter in this study. We found that size and brightness of the MBPs are significantly correlated. Our analysis also revealed a direct correlation between lifetimes and maximum intensities of the studied MBPs.

Chapter 1

Introduction

1.1 Background

Magnetic bright points (MBPs) are one of the manifestations of solar magnetism which exist in all regions and layers in the solar atmosphere. MBPs appear in the form of bright point-like features with some kG magnetic field strength ([8], [53], [50]).
Due to the concentration of magnetic field, the magnetic flux tubes are evacuated from hot plasma ([53], [50]), and consequently, evacuation lowers the optical depth inside the tube and hotter gas radiates excess energy. The walls at deeper optical depth are hot. This is because the temperature increase rapidly with depth below the solar surface. Therefore, the flux tube's walls radiate releasing the excess energy. Observing the walls at limb, MBPs appear bright([52], [16]).

The first observations of MBPs were reported by ([12], [31]) at disc center. For the past three decades, the MBPs properties and behaviors have been studied in different regions and heights ([4], [27], [41], [59], [26] , [25], [21]). The physical and dynamic properties of MBPs in different heights such as, e.g., the heights corresponding to G-band as well as Ca II K [25] and H [21] are studied.
A mean size of 166 km in G-band with a resolution of 0.054 arcsec/pixel was reported by [59], also a mean size of 150 km with a resolution of 100 km at the upper photosphere/lower chromosphere as well as the lifetime of a few minutes were obtained by [21]. A mean horizontal velocity of 2.2 km/s is reported by [21].

It is thought that MBPs' foot points non-oscillatory motions in the solar atmosphere can be important for generating magnetohydrodynamic (MHD) waves such as Alfven waves [9] [23] as well as energy transportation along the flux tubes from the photosphere to the corona to be responsible for coronal heating ([33], [34], [35]). Although, it is investigated that MBPs dispersal motions are important in diagnosing the photospheric vortices locations and spicules oscillations [22]. Therefore, measuring the velocity, size, intensity, and lifetime of MBPs, which can describe their properties, are the subject of this thesis.

1.2 Structure of thesis

We start with a brief introduction of the different atmospheric layers of the sun in chapter 2 (section 2.1, section 2.2) , followed by a short discussion about solar magnetism in section 2.3, where we discuss the generation of the solar magnetic field in different scales. The magnetic bright points (MBPs) which are the magnetic features under investigation of this study are described in section 2.4. The datasets, which are analyzed in this study, are introduced in chapter 3. The methods used to analyze the data are described in chapter 4. In chapter 5, the results are presented, with some discussions. Finally, we summarize our study and present the conclusions of this investigation.

Chapter 2

The Sun

The sun is a G-type main-sequence star with a surface temperature of about 5,770 K [37]. The solar system is located inside one of the milky way's galaxy arms. The sun was created from interstellar cloud compression during rotation. Two forces, gravity and pressure gradient act in opposite direction to keep the sun's balance.

2.1 Solar interior

The solar interior consists of the solar core, the radiative zone, and the convective zone. In the solar core, the temperature reaches up to 15 MK, the density is 1.6×10^5 kg m^{-3}, and the material is thoroughly ionized. The core radius is about 0.25 $R_\odot$. The sun generates most of its energy from the fusion of hydrogen to helium in this area [37].

Moving outwards from the core, the next layer is called radiative zone. It expands until $0.7R_\odot$. The energy generated in the core travels in the form of electromagnetic radiation through the radiative zone. The released photons interact many times as they pass through the dense medium. Therefore, the photons have a large mean-free-path length and it takes about a hundred thousands years for one photon to reach next layer. The density and temperature drop quickly, moving outward in this zone.

The convection zone is the next layer, a photon passes after its long journey through the radiative zone. In the convection zone, the gas temperature is less than 1 MK, and the opacity increases. The temperature variation increases in the opaque plasma and raises the instability in the medium. A portion of hot gas, in order to keep the stable equilibrium, moves upwards. In the surface, the opacity is reduced due to radiation from the solar surface. The plasma lifts upward, flatten on the surface (low photosphere), radiates photons, cools down, and descends. The process continues and this zone is called convective zone. The different flows which generates the convective zone play an important role in the formation of different waves in the upper atmospheric heights.

2.2 Solar atmosphere

The solar atmosphere comprises three different layers. The photosphere is a visible layer, what in fact is seen with naked eyes. The two upper layers, i.e., chromosphere and corona, also transion region which is placed between chromosphere and corona, can only be seen during a total solar eclipse when the photospheric gleam is darkened by the Earth's shadow.

The temperature and density stratification of the solar atmosphere are derived for a plane-parallel atmosphere is presented in figure.2.1, [63] [2]. The values are a fairly good approximation for the average quantities.

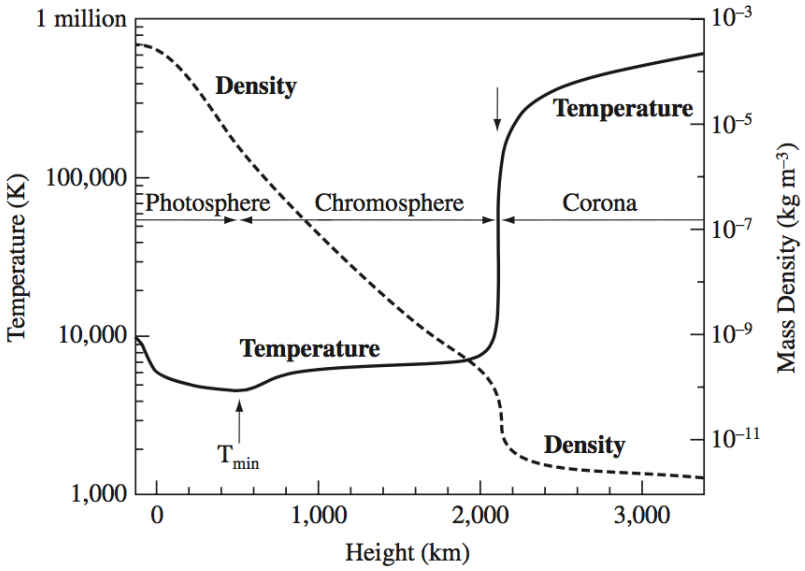

Figure 2.1: The temperature and density variation of the solar atmospheric as a function of height derive from the VAL model, [63], courtesy of Eugene H. Avrett.

2.2.1 Photosphere

The lowest region of the solar atmosphere is the photosphere. It extends about 500 km above the solar surface with temperatures between 4,000 to 6,000 K. The optical thickness is, on average, $\tau \lesssim 1$ for the visible, infrared, and near ultraviolet wavelength range (the optical depth for 500 nm light is one). Since, the temperature varies dramatically, the local thermodynamic equilibrium approximation (LTE) is applied to describe most of the lower photospheric conditions.

The sun is classified to be a cold star. We see that the main electron density in the photosphere is allocated to heavy metals which have low abundance, Since, the temperature in the photosphere is lower, free electrons bounce to hydrogen atoms and the H^- ions

produced and dominate in the photosphere. Thus, the solar continuum forms in this area. The energy transmission occurs in a form of convection and radiation. The so-called photosphere is made up of granule with a diameter of about 300 km to 2,000 km with various shapes [37] and lifetimes of order of 5 min [55]. Hot material is carried out upwards from lower layers to the surface where it gets cold. The cold material sinks back into the sun at the edges of granules that are so-called intergranular lanes. These are darker compared to hot granules. The photospheric granulation pattern presents the upflow in the center and downflow in the intergranular lanes. Granules can also originate from fragmentation of one larger granules or the merging of two or more smaller ones.

A supergranulation pattern appears in a larger scale than granulation. Its size is between 20,000 to 70,000 km [38] and reveals the horizontal flows from its center to its boundaries. The plasma ascends from the center and descends in the edges. The supergranules can be generated between the older cells, or by fragmentation as well as separation of the existing cells. The horizontal motions represent diverging pattern. The temperature in the center is higher than the boundaries [32]. Reversed granulation is the reversal of the continuum granulation pattern as observed, e.g., in the Ca II H and K lines. It shows a similar pattern than the surface granulation, but with reversed intensity contrast. So far, it has been explained in terms of convection reversal, atmospheric gravity waves or acoustic waves [40].

2.2.2 Chromosphere

As it is illustrated in Figure 2.1, the second solar atmospheric layer starts at a height of about 500 km corresponding to the temperature minimum 4,000 K and reaches up to 2100 km with temperature of 10,000 K. This layer is observable during the first few seconds of a total solar eclipse in the red Balmer spectrum at the solar limb. The colorful appearance of the solar limb is the reason calling this layer "color sphere" or chromosphere [37].

This part of the solar atmosphere is extremely inhomogeneous and highly dynamic in nature. It is transparent to near-infrared continua, visible, near-ultraviolet solar spectrum but, optically thick in strong spectral lines mostly emission lines as $H\alpha$, Ca II. This highly dynamic zone is dominated by small scale waves especially in internetwork regions which are a great part acoustic waves with a three-minute period formed by the convective motions ([40]).

The outward temperature increase and density decrease results in a break the LTE approximation in chromosphere. Chromospheric features include Ca II bright $k2v$ grains .i.e. non-magnetic feature in internetwork atmosphere, spicules (plasma jets), filaments (quiescent and eruptive).

2.2.3 Transition region and corona

The transition from cold plasma $T \approx 10^4$ K to a very hot plasma with temperature $T \approx 10^6$ K happens in the so-called transition region. This layer expands about 100 km and located between the chromosphere and the corona. This part of atmosphere is fully ionized and dominated by emission lines that emit the UV and in X-ray spectral range.

The tenuous corona with $T \approx 10^6$ K expands from the transition region into the interplanetary space with the solar wind. The high temperatures in corona provide an environment where atoms are completely ionized. The corona is seen at the eclipses (or where using a coronagraph) as a bright crown surrounding the sun. Coronal structure includes the dark coronal holes, bright coronal loops, and X-ray bright points. Some coronal features such as solar winds, flares, as well as coronal mass ejections, and helmet streamers, impact the Earth atmosphere.

2.3 Solar magnetism

To open the discussion about the solar magnetism, it is appropriate to start with the small and large scales flows which are responsible for the generation of the magnetic field, although, there are some complexities and coupling between both scales.

Since the angular momentum is conserved, the convection in the sun causes the solar global rotation called differential rotation. The sun does not rotates as a rigid body, but it rotates with different speeds at different latitudes.The upper latitudes rotate slower than the equator. The equator has the lowest period while is about 26 days and poles rotate in a period of 30 days. The differential rotation inserts different stresses in the convection zone as well as poloidal and toroidal flows [37].

In addition to the differential rotation the plasma flows slowly from equatorial regions towards the solar poles in a shallower layer of the convection zone and the flow returns in greater depth. This so-called meridional flow is considered to be important in flux transport theory and for the solar dynamo. The detection of this flow has its own difficulties due to slow migrations (speed about 20 m/s) [13]. At the bottom of the convective zone, there is a thin shear layer named tachocline which links the solar interior to the convection zone. It is thought that the tachocline is the source of the azimuthal magnetic field generation ([36]).

The solar interior spins rigidly, whereas the convection zone rotates differentially. This leads to change of angular velocity of the plasma in the solid solar interior and generate instability in lower convective area.
Variation in the plasma's structure and angular velocity can drag out buoyant magnetic field lines and make it very complex. This is called ω dynamo (the large poloidal emerged flux rooted in differential rotation). Due to convective instability the generated magnetic flux with company of small scale photospheric flows (granulation and supergranulation)

help the buoyant flux to raise up to the surface. The emerged flux appears as an $\Omega-$loop extending outwards. As long as the $\Omega-$loop moves out of the tachocline it is essential to substitute that with the amount of gas insert to the tachocline, therefore in the shear of tachocline the poloidal fields form and it produce the azimuthal field to improve or suppress the present magnetic field.
The foot-points of emerged flux on the surface represente bipolar or unipolar regions depending on where they are associated with open flux lines or closed loops. The exerted forces such as Coriolis force, twist the $\Omega-$loops, thus creating sunspots on the solar surface ($\alpha-$dynamo). Various interpretations and models describe the so-called $\alpha\omega-$dynamo and consequently the solar dynamo, but in summary all the mechanism which consist of the above processes, and also different suggested models to generate and expand the solar magnetism are referred to as the solar dynamo. ([36])

2.3.1 Solar magnetic small and large scales

The photospheric magnetic field gives important information that is crucial for better understandin of, e.g., local solar dynamo or coronal heating. Different regions possess specific magnetic strength and scale, also display certain attribute as various visual features. The whole solar surface is covered by emerged magnetic flux which they are renewed every 10 to 40 hours [37], therefore the solar surface have to be divided into different regions in magnetic points of view. Active region, quiet sun, and polar field are regional divisions based on the strength of the solar magnetic activities.

Active regions are large scale areas usually with opposite polarity extending from 45 degrees north and south of the solar equator. They represent regions of the emerging flux with high magnetic complexities and average magnetic field of several hundred Gauss. They include groups of sunspots, and pores, which are the foot-points of the emergent flux tubes smaller than sunspots, but larger than bright points without a penumbra. In photospheric magnetograms, active regions appears as very large white and black patches. As the solar cycle progresses, they appear on lower and lower latitude on the solar disk towards the equator. The preceding part is the eastern one and the following spot usually placed in the western part.

During the solar cycle the strength of the magnetic field varies. In the solar maximum, the active regions expand wildly as well as increasing in size and lifetime of sunspots.The formation of the active regions takes less than five days. Now active regions appear either near the old active regions or the remnants of them, after about 15 days they reach the peak of their activities. ([37])

In chromosphere, active regions can be described in Hα as stringy, long, thin fibrils and very bright areas called plage, which are intense emergence flux tubes surround sunspots and pores. It is assumed that fibrils outline the chromospheric magnetic field and track open flux to higher atmospheric layers [51]. Observations in Hα 6563 $\mathring{A}$ and He I 10830 $\mathring{A}$ demonstrate dark, cool, thread-like features called filaments in the solar disc (prominence

in the edge). They are very eruptive within the active region belt, in particular, in the solar maximum. The eruptive filaments have strong irregular explosion which sometimes eject plasma to corona.

In the upper atmospheric layers (corona and transition region) EUV and X-ray loops outline the large-scale structure of the magnetic field. Coronal active region have extremely hot temperatures rising up to 3 MK in the center ([37]).
Coronal mass ejections and flares are the eruptive features in the corona leading to large expulsions of material which occurs due to a sudden huge energy dismissal. Flares are notably observable in the X-ray particularly in young and well-developed active regions.

In the view of magnetic activity, large regions at the solar surface appears magnetically non-active. They appear as a gray carpet in magnetogram images. But, high resolution observations clarify that the solar surface is comprised two sub-regions known as network and inter-network.

The network is localized in the boundaries of supergranules and is associated with its horizontal plasma flows. Investigations of the photospheric small scale patterns have revealed that the plasma, in results of convection motion, tends to shift from the center of the supergranules to the sides. In photosphere, the magnetic field is usually influenced by the plasma motions. As plasma moves outwards simultaneously drags the emergent flux from the inside of super-granules towards their boundaries. Magnetic flux tubes accumulate in this area, leading to intense kG flux tubes that are distributed in the network.

The internetwork is situated in the supergranules interior area among network patches. In fact, the internetwork is perfectly large area consist of granules and intergranular lanes. It may be assumed that the magnetic field in this sub-region is less than network, but recent studies have elucidated that the magnetic field strength in the internetwork can be very strong and that the majority of magnetic field in the internetwork is recognized to be strong horizontal fields. [66]
The north and south pole of the sun are known as polar fields which are parts of quiet sun and do not show a very strong magnetic activity.

2.4 Magnetic Bright Points

As discussed 2.3.1, the small-scale magnetic field in the photosphere is not distributed uniformly everywhere. The horizontal plasma motions sweep the field lines toward intergranular areas where the small scale magnetic flux concentrations are formed. Such bundles of magnetic field lines are interpreted as photospheric thin flux tubes with kG field strength and spatial scales of 150 km, on average [21]. The flux tube theory [52] explains the mechanism under which these tubes are formed. This is summerizes in the following [49].

The magnetic force inside the bundle evacuates the tube. The pressure inside and outside the bundle are related by

$$P_{out} = P_{in} + \alpha B^2, \tag{2.1}$$

where α is a constant factor and B the magnetic field strength inside the tube.

The flux tubes form in the dark, cold, narrow corridor between granules. If the radius of flux tubes is less than or comparable with local pressure scale height (H_p), we consider these tubes as thin flux tubes. In this theory, we assume that the magnetic field outside of the flux tubes is zero ($B_{out} = 0$), and also each atmospheric level is isothermal everywhere. Therefore, hydro-static equilibrium applies for gas:

$$P = P_0 \exp(-\frac{z}{H_p}), \tag{2.2}$$

$$B = B_0 \exp(-\frac{z}{2H_p}) \tag{2.3}$$

where P_0 and B_0 are the gas pressure and magnetic field at $z = 0$.
Along the thin cylindrical tube, we assume that the magnetic flux (the magnetic field strength times the area including this magnetic field) is constant with height. Therefore, any reduction in magnetic field strength increases the area. Since, the gas pressure as well as magnetic field falls off exponentially with height in the solar atmosphere (in equation 2.3, 2.4), the cross section of the tube has to expand exponentially with height due to the assumption of conservation in magnetic flux. The thin flux tube foot-points inside cold and dark inter-granular lanes gleam as bright point-like photospheric features.

The excess brightness in MBPs observed in the upper photosphere/lower chromosphere is, however, different. In particular, intensity of MBPs in Ca II H passband have strong contribution through emission peaks around the line core of this line (due to enhanced population density as a consequence of, e.g., line-radiation and acoustic waves.)

The generated MBPs observed bright in high resolution intensity images, such as the one is shown in the Figure 2.3. They are referred to as magnetic bright points (MBPs). This image is taken from the time-series of images of the Fe I 6173 $\mathring{A}$ dataset which is analyzed in this study (see chapter 5).

Chapter 3

Data

The objective of this chapter is the introduction of the datasets that are used in this investigation and were recorded at Swedish Solar Telescope (SST). The design and optical layout of the SST is described in detail in ([44] and [47]). In following, we adopt these works to describe the optical system of the SST (section 3.1).
The datasets which are described in section 3.2 include observations in Fe I 6302 $\mathring{A}$ wideband, Fe I 6173 $\mathring{A}$ wideband, Fe 6302 $\mathring{A}$ line core, and Ca II H.

3.1 The Swedish Solar Telescope (SST)

The SST is a vacuum optical telescope with a remarkable resolution of 0.1 arcsecond. It has been built on the island of La Palma in Spain at an altitude of about 2400 meters above sea-level, in a 17 meter high tower. The SST mechanical design includes the assembly, the turret, the telescope servo system, cooling and baffling systems, and the corrector system mechanics. In addition, the optical system includes the primary optical part, the Shupmann corrector, and the adaptive optics system.
In order to correct the effects of the aberrations from atmospheric dissipation and longitudinal or traverse chromatic aberrations, a corrector Schupmann achromat is used as well as a re-imaging system with commutable and adaptive optics.The design of the SST is flexible for further upgrades. In the following, we briefly describe the optical system as well as the instruments used for observing the data that has been analyzed in this study.

3.1.1 Optical system

In figure 3.1, we show a sketch from [44] which gives an overview of the SST assembly, design of the tower, turret, and optical elements.

The primary optical elements are positioned on the top of the SST tower at the entrance of the beam. They include a 1-meter diameter fused silica singlet lens with a 0.97

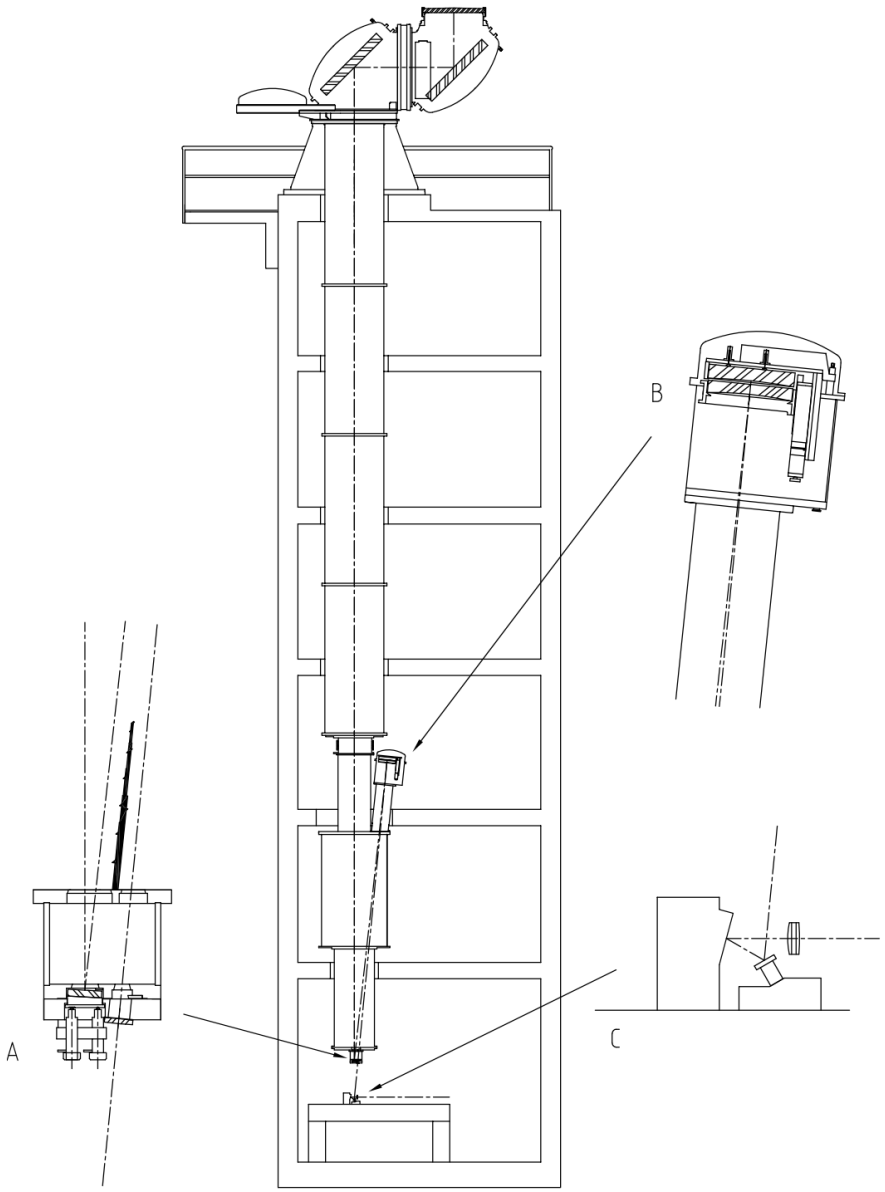

Figure 3.1: The sketch illustrates the main tower of the Swedish Solar Telescope (SST) with its turret and vacuum system and the primary optical setup on top. In panel A, a field mirror and field lens are shown. Panel B displays the Schupman corrector. Panel C shows the adaptive optical system consisting of an adaptive mirror (deformable mirror), a tip-tilt mirror, and a re-imaging lens. Courtesy of [44].

m clear aperture and two 1.4 m flat mirrors with a thickness of about 150 mm.
The objective lens has a focal length of 20.3 m at a wavelength of 460 nm with a thickness of 82.4 mm in the middle. The lens has a low-temperature sensitivity, i.e. a low thermal expansion coefficient, which prevents stresses in the lens due to temperature fluctuations. The silica lens is placed on a short cylindrical box to protect it from heating of the straight sunlight.

The Schupmann corrector which is represented in figure 3.1B, includes a negative lens and a mirror. It corrects the achromatic aberration of the singlet lens. According to [44], the corrector system decreases the atmospheric perturbations by a factor 15-50 depending on the wavelength interval which is very good in the range of visible to UV and good for NIR wavelengths.

Adaptive Optics (AO)

The purpose of designing an adaptive optics system is to reduce imperfections due to atmospheric distortions in the ultimate images. The correction of an image is possible by considering the distortions of incoming wavefronts in the atmosphere and reversely distorting the incoming wavefront in the AO system. Figure 3.1C shows the re-imaging optics consisting of a tip-tilt mirror, a deformable mirror, and a re-imaging lens. The tip-tilt mirror corrects large-scale shifts of the incoming light and the deformable mirror operates with 85 actuators.

The AO system uses the wavefront sensor which is measuring the aberrations of the incoming wavefronts. It consists of hexagonal elements which fit with the geometry of the adaptive mirror. The wavefront sensor is placed in the red beam following the dichrioc beam spliter.
In addition, the correlation tracker monitors the image motion to adjust the tip-tilt mirror for further corrections. The different components of the AO system are shown in figure 3.2, which is taken from [11].

3.1.2 Instruments

The instruments that have been installed at the SST are the imaging CCD (charge-couple device), different filters (in the range of 380-860), a spectrograph (for the purpose of multi-wavelength observations, the slit unit is capable to change the size of the focal plane and using the spectro-polarimetry), a Doppler-graph, and a polarimeter. Also, the Crisp Imaging Spectro-polarimetry (CRISP) [43] was installed at the SST in March 2008, [48].

Blue beam

As shown in figure 3.2, the incoming light from the AO system passes through a dichroic splitter which separates the beam into a blue and a red beam. As described in [18], on

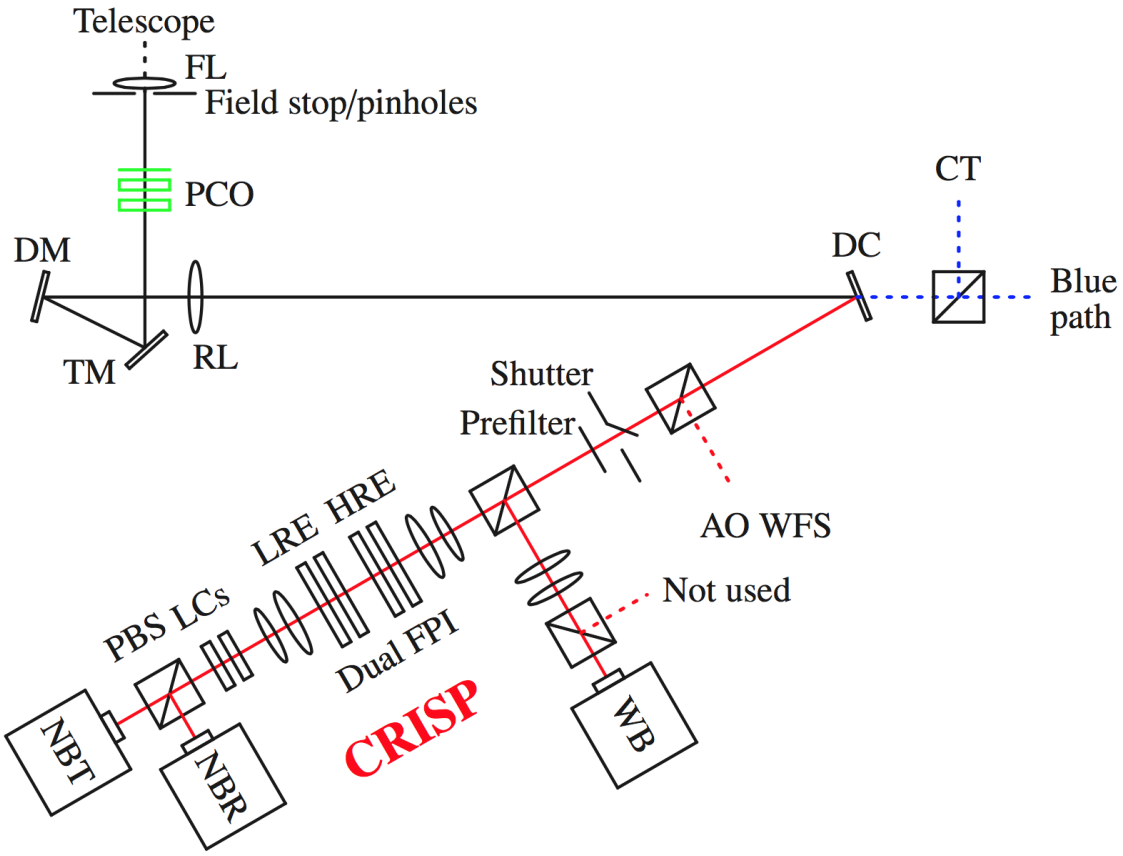

Figure 3.2: Sketch of optical setup of the SST. The abbreviations in the figure are: FL= Field Lens, PCO = Polarization Calibration Optics (not in the beam during normal observations), TM = Tip-tilt Mirror, DM = Deformable Mirror, RL = Reimaging Lens, DC = Dichroic Beamsplitter, CT = Correlation Tracker, AO WFS = Adaptive Optics WaveFront Sensor, FPI = Fabry Pérot Interferometer, HRE = High Resolution Etalons, LRE = Low Resolution Etalons, WB = Wideband image, NBT = Narrowband Transmitted, NBR = Narrowband Reflected image, LCs = Liquid Crystal modulators, PBS = Polarizing Beam Splitter. Courtesy of [11].

the blue side of the beam, a tiltable filter camera, a wideband camera, a fixed wing filter camera, and a wideband phase diversity camera are aligned on the optical axis. While the blue light passes through the blue tower setup, it is divided into two parts. The major part of the light passes through the tiltable filter, therefore providing a remarkable SNR for the line core images. The other part goes towards the three cameras (If they are all used). Fifty percent of the original blue beam reaches the second spliter.

This beam separator sends one part of this beam to the fixed wideband camera and the rest to a line core filter camera, e.g, the Ca II K line core filter or a line wing filter. The last two cameras provide wideband images from the rest of 25 % of the light, while one of them provides the wideband phase diversity images for the image restoration purposes. Also, an interference filter is between the two last beam spliters. This filter separates a bandwidth of the near continuum between Ca II K and H lines.

Red beam

According to figure 3.2, Crisp Imaging Spectro-polarimetry (CRISP) [43] is installed in the red beam.
As figure 3.2 shows, before the beam enters the CRISP instrument a chopper wheel synchronizes the cameras along the light path. Afterwards, the beam enters a filter wheel with various prefilters which obtain different spectral lines with the FWHM in a range of 0.3-0.9 nm. They can be adjusted in a few hundred ms during observations.
The red beam is split again after passing through the filter wheel by a beam splitter. One part goes towards a wideband camera, the main part of the red beam keeps the straight light path through a dual Fabry-pérot interferometer (FPI) system.

The FPI acts as an adjustable narrowband filter which moves a transmitting narrow band filter to a new spectral line position. It includes two etalons. Every etalon has two parallel reflecting surfaces, one with high spectral resolution and high reflectivity, the other with a low resolution and low reflectivity. To minimize the stray light errors due to multiple light reflections inside two reflectors, the etalons have been built as compact as possible.

The polarization modulation is installed after the FPI. The polarimeter at the SST comprises a pair of liquid crystals (LCs) which are tunable and placed in the beam. The first one is parallel to the vertical polarizer filter and the second one is aligned 45° relative to the vertical axis of the first LC, in order to measure the four Stokes parameters (I, Q, U, and V). A linearly polarizing beam-splitter divides the beam into two horizontal and vertical components. Afterwards two separated beams enter the reflected and transmitted narrowband cameras which allows to measure the two orthogonal polarization states simultaneously. The three Sarnoff cameras are synchronized, comprises of 1024 by 1024 pixels of 16×16 μm^2 and equipped with CCD detector technology.

Table 3.1: Summary of technical information of SST/CRISP datasets used in this study.

Quantity	Fe I 6302 $\AA$	Fe I 6302 core line	Fe I 6173 $\AA$	Ca II H
Spectral resolution [$m\AA$] [a]	54.8	54.8	50.7	1.0 [b]
Height of formation [km] [c]	60	120	60	820
Date of Observation	6 August 2011	6 August 2011	4 Jun 2012	6 August 2011
Cadence [s]	28	28	14	28
Time duration [min]	47	47	41	47
N. of frames	100	100	176	100
N. of W. positions	15	15	10	-

[a]The full width at half maximum (FWHM) of CRISP trasmission profiles from [11]
[b]This is the FWHM of the Ca II H through the narrow band filter in $\AA$.
[c]The mean height of formation. Provided by S. Jafarzadeh (Priv. communication)

3.2 Data

3.2.1 Observations

We refer to [20] for the datasets that are used in this investigation. They are high spatial and temporal resolution time-series of images of Fe I 6302 $\AA$ wideband, Fe I 6173 $\AA$ wideband, Ca II H, and Fe I 6302 $\AA$ line core observed with SST taken near the solar disk center in a quiet Sun region. In Table 3.1, information of the all datasets is summarized.

Observations of the Fe I 6302 datasets were performed on the 6th of August 2011 starting at 07:57:38 UT. Those for the Fe I 6173 $\AA$ dataset were performed on June 4th 2012 starting at 07:33:02 UT. The Ca II H dataset was recorded through the 1.0 $\AA$ narrow band filter at the same date as the Fe I 6302 $\AA$ wavelength, i.e., on August 6th 2011.

The images have been recorded with a scale of approximately 0.06 arcsec/pixel. The Fe I 6302 $\AA$ wideband, Fe I 6302 $\AA$ line core, and Ca II H datasets cover a 53×53 arcsec^2 FOV equivalent to 39,000×39,000 km^2. Each dataset consist of 100 frames with a cadence of 28 s which was recorded during 41 min.
Regarding the Fe I 6173 $\AA$ wideband, each FOV covers about 56×56 arcsec^2 or 41,200×41,200 in km^2, a cadence of 14 s, and with 176 frames recorded during about 47 min. The images that are displayed in figure 3.4 show examples of single frame intensity of the Fe I 6302 $\AA$ wideband, Fe I 6302 $\AA$ line core, Fe I 6173 $\AA$ wideband, and Ca II H datasets, respectively.

The formation heights for the Fe I 6302 $\AA$ wideband, Fe I 6173 $\AA$ wideband, Fe I 6302 $\AA$ line core, and Ca II H passband filters are 60, 60, 120, 820 km, respectively (see Table 3.1). The average formation heights for the four datasets (weighted by contribution functions [1] (CFs) [5]) is provided by S.Jafarzadeh (Priv.communication). They were obtained by

[1]The CF gives a function which provides the contribution of a range of given heights to form the emergent intensity (for the free-free and band-free processes) or the line depression (for the band-band

applying 1D RH-code which is based on the multi level accelerated lambda iteration and developed by [56]. were obtained in the non-LTE condition. The CF measurments for the Ca II H was based on the assumption that the filter was perfectly calibrated to the line center. The CF for the Ca II H line core is a delicate computation. Thus, this height (mentioned in Table 3.1) is its upper limit.

The computations were carried out at the FALP atmospheric model [14], which is a one-dimentional semi-imperical model that described plage regions. In an investigation by [21], the formation height of Ca II H was computed at different atmospheric models FALF, FALC, and FALP [15]. By comparing those three models, it turned out that the FALP model can can best describe formation height of magnetic bright points (that are features of interest in this study). Figure 3.3 shows the CFs of four passband filters which are over plotted for FALP atmospheric model.

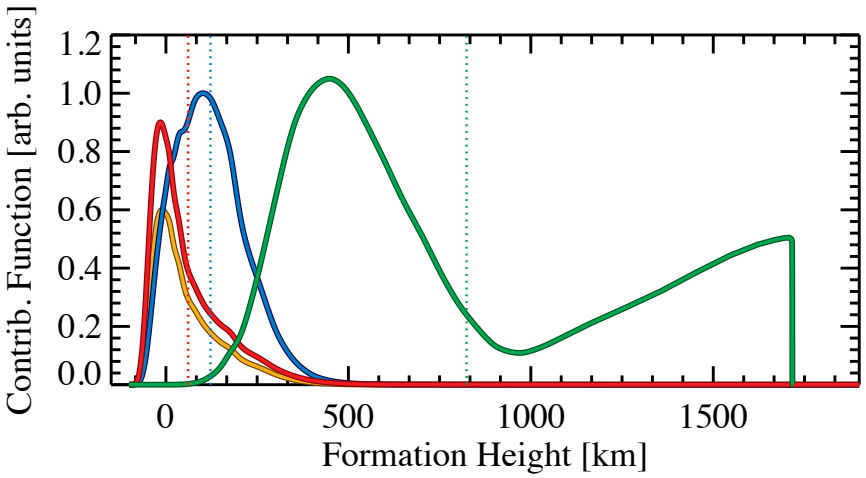

Figure 3.3: The CFs for the four datasets computed and plotted at the FALP atmospheric model by S. Jafarzadeh (Priv. communication). The Fe I 6302 $\mathring{A}$ wideband, Fe I 6173 $\mathring{A}$ wideband, Ca II H, and Fe I 6302 $\mathring{A}$ line core are represented in yellow, red, green, and blue color respectively. The vertical dotted lines show the corresponding average formation height for each dataset. The red and yellow vertical lines are coincided at the same position.

All images, excep those in Ca II H, were recordeded using the CRISP dual FPI by scanning of the spectral lines of the Fe I 6173 $\mathring{A}$ and Fe I 6302 $\mathring{A}$ in 10 and 15 line positions, with FWHM of 50.7 and 54.8 m$\mathring{A}$ of the CRISP transmission profile respectively.
The polarimetry was carried out in the LCs modulators of CRISP instrument and polarizer beam splitter operated to reduce the polarization crosstalk by simultaneous imaging the two narrowband and wideband cameras. Two Stokes V images for Fe I 6302 $\mathring{A}$ and Fe I 6173 $\mathring{A}$ are represented in figure 3.4, which were provided by averaging 4 and 2 wavelength positions, respectively.

The data was processed in the CRISPRED pipeline. According to [11], the processing starts with dark current and flat-field corrections, followed by polarimetric calibra-

processes).

tion, prefilter transmission and wavelength shift corrections. The images are then restored from wavefront aberrations by means of Multi-Object Multi-Frame Blind-Deconvolution (MOMFBD) ([62], [61]). The pipeline also includes different calibrations for the field and time dependent polarization, inner-camera and temporal misalignments as well as the corrections for image field rotation due to the combination of the Earth's rotation with the altitude-azimuth mounting of the SST, and corrections of the cavity errors during the image-processing.

3.2.2 Image Post-processing

The image restoration method that was applied is known as Multi-Object Multi-Frame Blind-Deconvolution (MOMFBD) technique, referring to ([62], [61]), the captured image consist of a convolution of the true image and a point spread function[2] (PSF), which represents effects of seeing and image-degrading effects from the telescope.

In fact, the MOMFBD by employing one extra step which is the multiple realization of the multiple objects and is restored jointly, extends the Multi-Frame Blind-Deconvolution (MFBD) method presented by ([28], [29]). Below three steps of the MOMFBD are described:

1. Blind-Deconvolution: reduces the PSF from the image and extract the true image with the assumption that the FOV is unchanged. This method provides a joint estimation of an object and aberrations and find PSF of an ill-posed problem with "blind" assumption on the PSF.

2. Multi-frame: refers to multiple frames taken from similar scenes, but with different distortions in variable seeing. It estimates the unaberrated object as well as the pupil phase aberrations responsible for blurring of the image. This is done partly in a maximum likelihood sense for multiple samples of seeing.

3. Multi-object: means that different cameras take different images simultaneously in the red beam using wideband and narrowband passband filters. This technique allows multiple realizations of multiple object to be jointly resolved.

[2]The PSF is the response of an optical system to a point source which degraded its original image by noises from the medium and optical system.

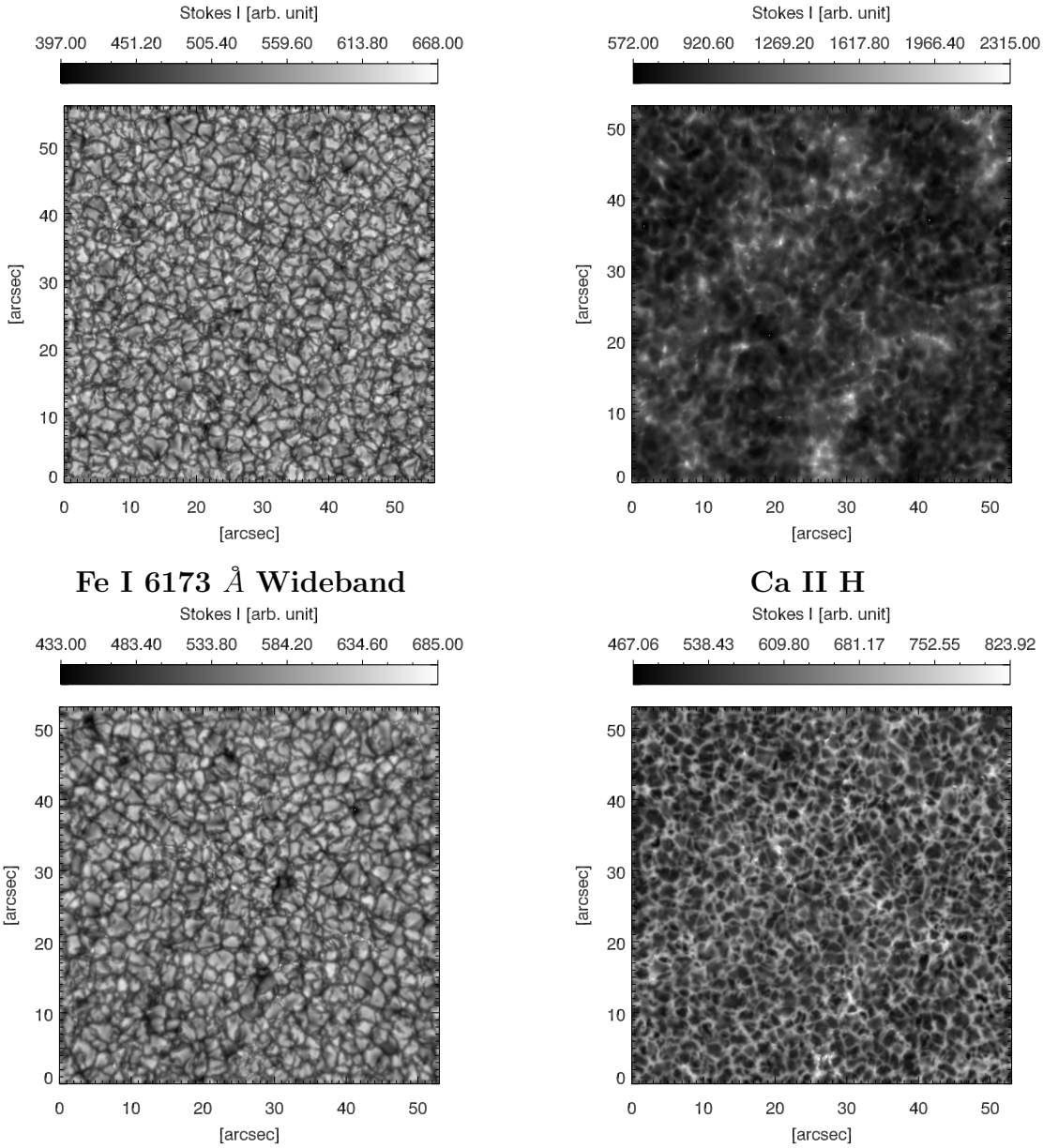

Figure 3.4: Single images of each dataset are represented. Every image shows the intensity of an area near the solar disk center in a quiet sun region. The FOV is 53×53 arcsec^2 for the Fe I 6302 $\mathring{A}$ wideband, the Fe I 6302 $\mathring{A}$ line core, and Ca II H datasets and 56×56 arcsec^2 for the Fe I 6173 $\mathring{A}$ wideband corresponding to a resolution of 0.06 arcsec/pix.

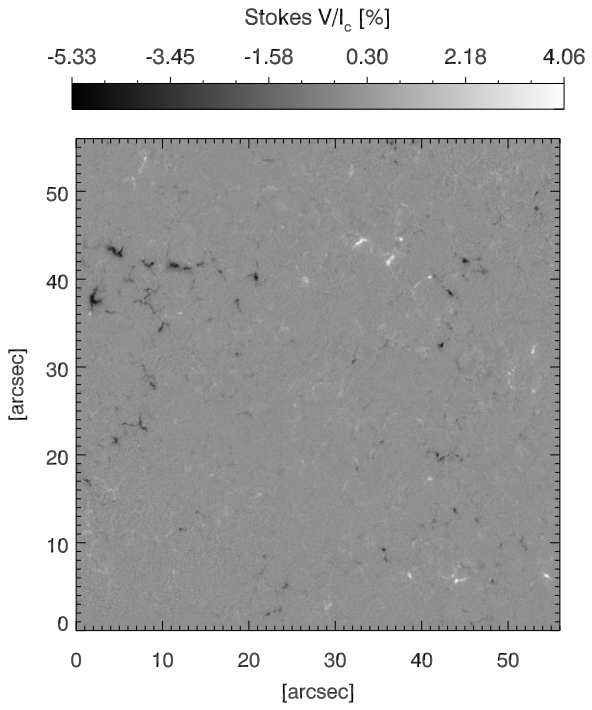

Fe I 6173 $\mathring{A}$

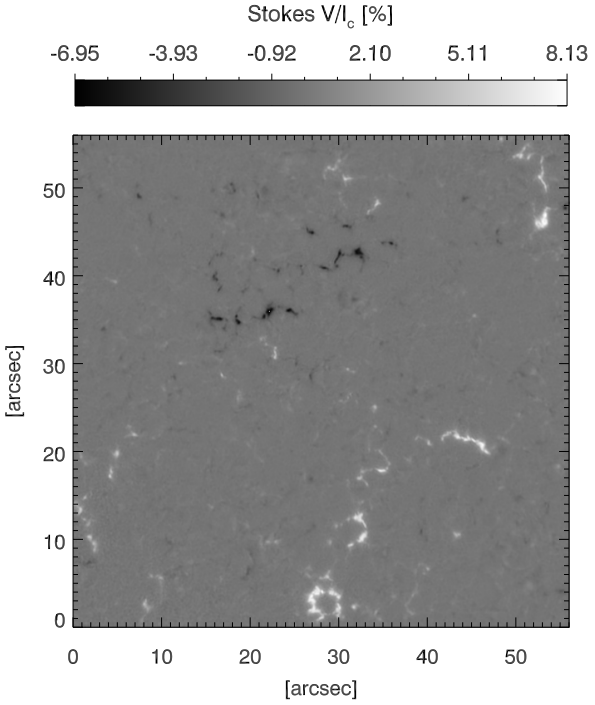

Fe I 6302 $\mathring{A}$

Figure 3.5: Examples of normalized Stokes V to Stokes I continuum for the Fe I 6302 $\mathring{A}$ (bottom) and Fe I 6173 $\mathring{A}$ (top) corresponding to the images represented in figure 3.3.

Chapter 4

Method and Analysis

We aim to study properties of MBPs observed in different passbands, sampling varius heights in the lower solar atmosphere. To this end, we use a semi-automated algorithm provided by S. Jafarzadeh (priv. communication). In this method, the MBPs candidates are selected manually followed by an automated detection using an iterative solution. The advantage of this approach compared to other fully automated algorithms is to prevent misidentification of, e.g. small granules that can be hardly discriminated from MBPs or other non-magnetic brightenings occurred in upper photosphere/lower chromosphere.

In this chapter, we discuss the event detection, which comprises events definition, selection procedure, and extracted physical parameters. The event definition acquires the assessment criteria for inclusion or exclusion of a chosen MBP.
In addition, a tracking algorithm is described using which the identified MBPs are traced during the course of their lifetimes. Finally, a number of physical and dynamical parameters of these MBPs are determined.

4.1 Event detection

Our event detection includes certain conditions from which MBPs are defined. Therefore, it is essential to define the evaluation criteria for the events about which we are going to investigate. The detection algorithm is based on these criteria which limits us to a specific group of bright features.

4.1.1 Event definition

The MBPs must satisfy particular criteria to be chosen, otherwise they are discarded. Below, we discuss the criteria that are considered to select a MBP.

- **Presence of magnetic field**: Stokes V signal as the LOS component of the magnetic field can ensure the magnetic characteristic of the candidate bright features. We employ a signal-to-noise ratio (SNR) of at least 3σ on the Stokes V signals. Hence,

one of the important conditions is the existence of Stoke V signal for a feature to be considered as a MBP.

- **Circular-shaped**:
  The targets are included if they are approximately circular-shaped features. However, the temporal evolution of a candidate feature during its lifetime can change its roundish appearance to a stretched ellipse, in which very long cases does not fulfill the assumed criterion.

- **Isolated MBPs**:
  The isolated features are defined as those that do not merge or fragment during the selection procedure.
  We point out that the chain-like points which appear to include separated MBPs are selected (it is discussed later). Figure 4.3 represents one example of chain-like MBPs. After fragmentation of a MBP into two or more bright features, the new MBPs are considered as new individual features.

- **Located in intergranular lanes (Ig)**:
  The Ig area is a place that MBPs are accommodated. All candidate features that we choose are located in this area.

The above criteria are considered as eligibility of MBPs to be chosen in this investigation. We note that other bright point-like features, such as Ca II H_{2v} and K_{2v} grains ([6], [7]), are also observed in the quiet sun internetwork regions, are not magnetic and hence, they are excluded.
Also, we notice that with the assumption of significant Stokes V signal i.e., with a SNR threshold of 3σ, we may miss MBPs with weaker magnetic signals.

4.1.2 Detecting algorithm

Detection of MBPs in this project is based on a manual selection, followed by further steps carried out automatically. The latter is based on the "blob analyzer "routine which provides a set of analysis for a selected MBP. As a result, physical properties of the selected MBPs namely, size and intensity, along with their coordinates are determined.

4.1.3 Selection Procedure

During this procedure, we have gone through each FOV by dividing every frame into four sub-fields of view (sub-FOV). We magnified every sub-FOV by a factor of 2 to facilitate the recognition of MBPs by the eyes.
In the following, we describe the selection procedure within two consecutive frames. The procedure is identical and performed repeatedly.
The selection procedure comprises three steps:

1. Selecting all visually found MBPs in the entire sub-FOV,

2. Clicking on each candidate in a smaller area with a size of 21×21 pixel^2, when the MBP selected in step (1) is approximately located in the center,

3. Manual decision for inclusion and exclusion of the automatically detected MBPs shown at the center of a 7×7 pixel^2 window.

Starting the code, two windows are plotted side by side. One shows the intensity image and the second displays the corresponding Stokes V map with contours indicating the 3σ noise level. We represent an example for the Fe I 6173$\mathring{A}$ wideband dataset in Figure 4.1.

Following the step one, a cursor, i.e., a small dot with a circle with a radius of 10 pixels around, is depicted as a pointer to click on the center of a target. For avoiding the edge effects, the code acquires a red-line with 10 pixels from the edges of the original frames. These side strips are excluded from our investigation.

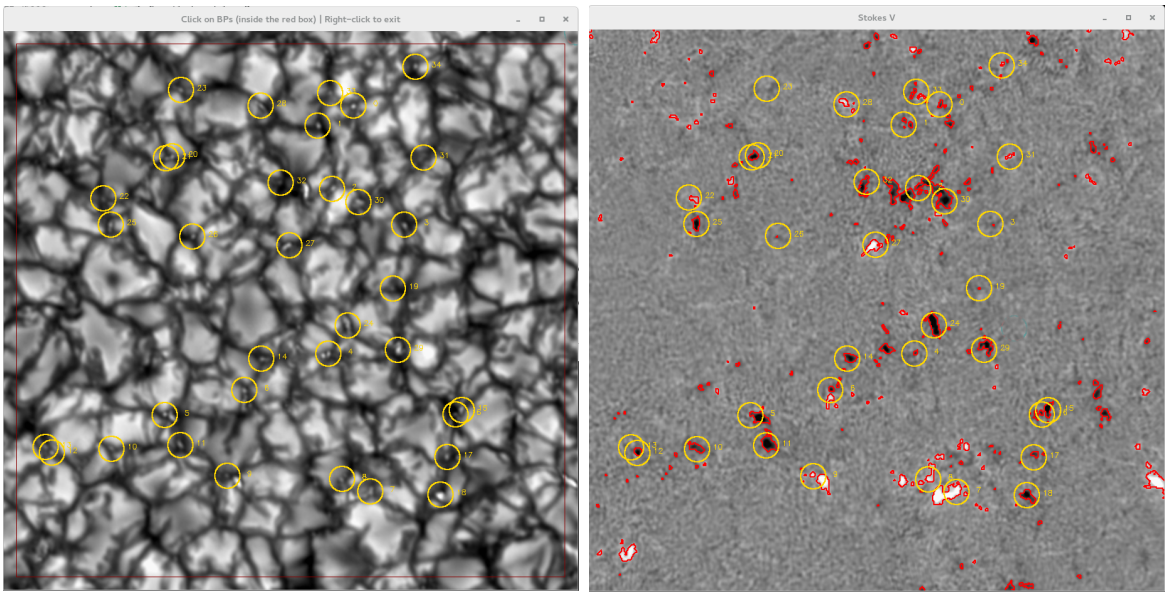

Figure 4.1: An example of a sub-FOV of the wideband image (left) and Stokes V map (right) of the Fe I 6173 $\mathring{A}$ dataset. The yellow circles represent a few selected MBPs on both images. The contours on the Stokes V map indicate the 3σ noise level .This is the first stage of the manual selection phase.

The cursor moves simultaneously in both windows. Hence, in case of any doubts about the magnetic characteristic of a selected bright point, it is possible to check its position in the Stokes V map. First step ends with choosing all possible visually identified MBPs in one frame.

Before describing steps two and three, it is useful to introduce two windows which are employed here. Every window consist of two images.
First window has a FOV of 21×21 pixel^2 and the second window has a FOV of 7×7

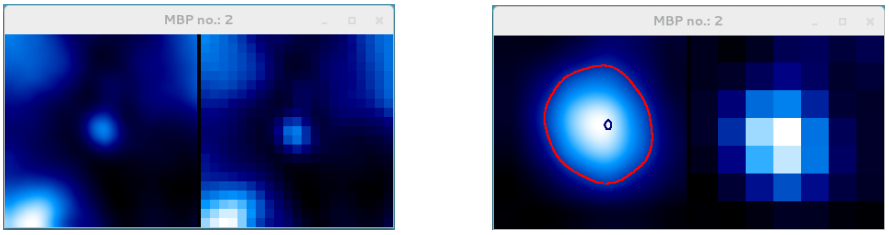

Figure 4.2: Examples of the second and third steps of our manual selection procedure for a MBP (left and right windows, respectively; see main text). Each window includes a smoothed (left) and original (right) images. This is an obvious example of an isolated MBP in Ig.

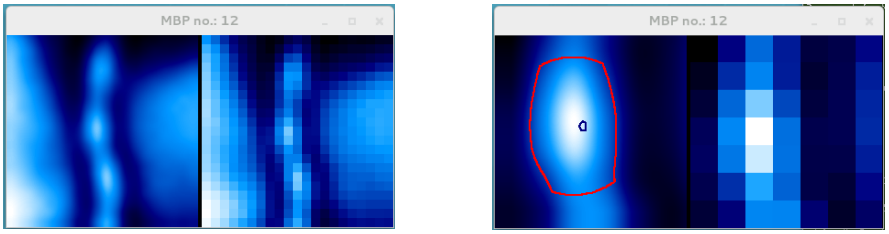

Figure 4.3: an example of a chain-like points. The brightness of each pixel in the original image ensures the separation of the MBP from its adjacent.

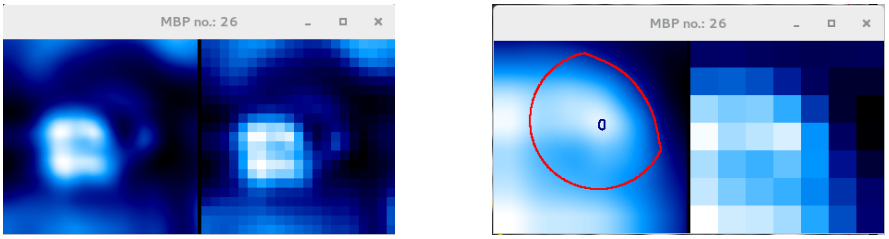

Figure 4.4: an example of a discarded MBP during fragmentation of a large MBP into 4 MBPs.

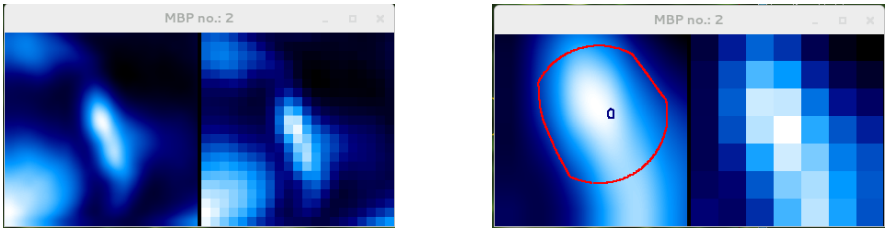

Figure 4.5: a discarded MBP due to merge of two adjacent MBPs.

pixel^2 of a scene which displays an area centered in the center of a candidate MBP chosen in our very first selection. One of the two images is an interpolated vision of the chosen MBP and the other one shows its real image in form of pixel's square-shaped. Figures 4.2, 4.3, 4.4, and 4.5 are four examples of different MBPs in the second and third steps of the manual selection.

In the second step, each pre-selected MBP is illustrated in the 21×21 pixel^2 size window. This facilitates identification of the MBP in a small area where other non-interesting brightenings are not shown. Here, the user should click on the feature to provide an approximate position to the automated detection algorithm. The ultimate selection in this stage is carried out in the interpolated image of the first window (usually is placed in the left side).
The third step begins with implement of automated detection, where coordinates and physical parameters are determined, followed by final selection of the MBPs' candidates.
To summarize, after manual selection of the MBPs in the first and second stages, the detection algorithm identifies chosen MBPs with the help of an iterative solution, and computes their statistics and parameters automatically. If they pass a final manual acceptance. The latter is done by user, judging from the last zoomed window (the 7×7 pixel^2 images). Features that do not seem to satisfy the pre-defined criteria are discarded in this stage.

After the first frame, the same procedure is repeated for the next frames. The only difference is that the selected MBPs in the prior frame is marked on the new frame (with dash circles). It is required to choose again all those MBPs if they have not disappeared to keep track in the sequential frames. Losing one MBP decreases the accuracy of our work and baises the tracking results. Meanwhile, if new MBPs appear in the image, we choose them as well.

4.1.4 Extracting Physical parameters

The accumulated information needs to be extracted from the stored files provided in detecting stage. What we have obtained so far are the parameters that describe every MBP properties within a set of images and also information needed for tracking purposes. Among the parameters that are determined and recorded, intensity, size, and position of each MBP are described in the following.

Coordinates

To acquire the position of a feature, the detecting algorithm measures the pixels value inside the area of a MBP . Coordinates of a pixel with maximum recorded intensity determines the coordinates of the MBP. If more than one pixel have identical maximum value, their half distances are computed as its location.

Size

In this research, we employ two methods to define the size of MBPs. One of them measures the size of MBPs in the detecting algorithm and the other approach acquires this quantity from the tracking code. Both approaches are explained below:

- The first method determines the size of a MBP with considering the FWHM of its maximum intensity profile. This concept is a technical term to specify the width of a feature without clear boundary in an image which is defined by the 2D Gaussian fit to the intensity profile.
  The alternative description implies the area that is accounted due to variation of intensity from the peak value to its half. Therefore, this definition gives a near circular pattern for the relevant MBP referring to the Gaussian distribution in which its mean FWHM provides the diameter of the circle with equivalent area. This approach has been applied for measuring the size of photospheric MBPs in the quiet sun region in [54] and [42].

- The next method describes the size of a MBP according to the approach described in ([10], [21]) which determined the intensity-weighted of pixels within a MBP. It is the root mean square (rms) of the intensity-weighted distances of all pixels inside a MBP from its center. The location in this method is based on the center of gravity intensity within a MBP. We take this alternative interpretation for measuring the center of a MBP in tracking procedure, as it was also used in [21].

Brightness

MBPs are searched in the dark intergranular lanes with relatively high local intensity contrast. The total intensity of the each MBP is measured as the total pixel values inside the feature. It is measured during detecting algorithm as well as tracking algorithm. The brightness of each MBP is also determined in three regimes as maximum, total, and mean intensity. We normalize the obtained intensities with the mean image intensity of their corresponding frame $< I_{QS} >$ for each dataset individually.

4.2 Tracking algorithm

We use an automated tracking algorithm to track the detected MBPs during a set of subsequent images. This algorithm provides a systematic function to measure the location of each MBP during its lifetime. It is essential that the tracking algorithm can support the changes which occur in the shape of the features and their other parameters during the tracking steps.
The method that is used in this work to pursue identified MBP, can track BPs in a very variable and noisy medium. This algorithm is explained in detail in [21].

We prepare a set of images that only include the identified MBPs (i.e, empty frames filled with the detected MBPs). We apply the tracking algorithm on these images where no other brightenings can interfere the tracking procedure.
During the tracking steps, the algorithm measures the tracked MBPs quantities. The recorded parameters in this method are coordinates, size, and intensity. In addition, the other quantities of MBPs that are determined due to their mobility are lifetime and horizontal velocity in this project. Obviously, the number of dynamic MBPs, refers to the features that last more than one frame, is less than the number of total identified MBPs.

Here, the dynamic detected MBPs are tracked from the first frame of existence to the last one. The tracking procedures are continued until a MBP does not meet the criteria in tracking. This method comprises trajectory of each MBP by linking their coordinates in consecutive frames.

The precise coordinates of each MBP in the tracking procedure is measured as following: a circular frame is defined which its size is slightly larger than a typical maximum size of the MBP. The center of this circular window adapts the center of the candidate MBP. The pixels value inside the circular frame determines its intensity center of gravity as the new coordinates for the MBP. Thus, the center of the circular window sits in the new position. The described operation is repeated during the procedure for all MBPs and their regarding windows. It is also continued by measuring and revising the position of the assumed frame to find its offset from the present location. Measuring the offset is iteratively computed to find the best estimation.

The next stage is linking the selected MBPs in the consecutive frames. The closest MBP in the new frame to the location of the chosen MBP in its initial frame is identified automatically by comparing their coordinates in both past and present frames. Linking the coordinates provides the trajectory of a MBP during its lifetime as well as other parameters such as horizontal velocity. This operation continues repeatedly across the frames of a dataset and measures the parameters of MBPs, for both dynamical and physical quantities.

4.2.1 Dynamical parameters

The MBPs properties are classified in physical and dynamical parameters . The dynamical features are tracked frame by frame to obtain their dynamical parameters such as lifetime and horizontal velocity.
Measuring the lifetime for each candidate MBP is a challenging subject which involves with different uncertainties. The horizontal velocity computation can be also influenced by the accuracy of acquisition of the lifetime. In the following sections we discuss those contexts.

Horizontal velocity

To clarify the meaning of horizontal velocity, we should mention that it refers to the velocity of a MBP in the surface perpendicular to the line of sight direction (LOS). The z-axis is assumed the LOS direction. The horizontal velocity is considered in two components along the x and y axes. Therefore, the horizontal velocity is computed according to the horizontal displacement of one MBP across two uninterrupted frames, dividing by the time between them. It is interpreted as an instantaneous horizontal velocity, i.e, a frame to frame velocity. Also, the average horizontal velocity is computed which explains the mean horizontal velocity of a MBP during its journey.

Lifetime

Obtaining the lifetime of MBPs accurately in the certain heights in the solar atmosphere and different regions ([24], [1]) can be a challenging issue due to define the birth and dead time for a MBP. The duration between the appearance (birth time) and total absence (dead time) for one MBP is known as its lifetime. Thus, the method that one may use to select, detect, and track MBPs during time steps can strongly affect the results and consequently on measuring the dependent parameters.

Chapter 5

Results

In this chapter, our results are presented followed by some discussions and plots quantitatively and qualitatively.
First, we discuss the obtained results from the extracted physical parameters of the MBPs observed in Fe I 6173 $\mathring{A}$ wideband, Fe I 6302 $\mathring{A}$ wideband, Fe I 6302 $\mathring{A}$ line core, Ca II H passbands.
Later, the outcomes of the dynamical properties of MBPs are discussed. We display the distribution of the lifetime and horizontal velocity parameters of four groups of MBPs related to four datasets. Then finally, study of correlations between parameters is provided.

5.1 Statistics of Extracted Physical Parameters

5.1.1 Intensity

We obtained the brightness of the detected MBPs in three regimes such as maximum intensity, average intensity, and total intensity. They are normalized to the mean image intensity of each frame corresponded dataset individually.

As shown in Table 5.1, brightness of the detected MBPs in the two wideband datasets (i.e., Fe I 6173 $\mathring{A}$ wideband and Fe I 6302 $\mathring{A}$ wideband) behave almost identically, while the brightest of the MBPs observed in the Ca II H and then Fe I 6302 $\mathring{A}$ line core have mean intensity of $3.6< I_{QS} >$ and $1.9< I_{QS} >$, respectively. The results indicate that the Ca II H MBPs have the largest intensity variation among all other MBPs observed in the other three datasets.
In addition, the minimum value of the mean, maximum, and total intensities of the observed MBPs in the four datasets are approximately equal to their mean image intensity of each frame, with the exception in the minimum total intensity of MBPs observed through the Ca II H and Fe I 6302 $\mathring{A}$ line core passband filters (i.e, 11 and $13< I_{QS} >$, respectively). The standard deviations of the mean intensity for the four datasets are calculated identical with the corresponding maximum intensity. But, this value differs from the obtained

Table 5.1: The quantitative information of the physical and dynamical parameters of the MBPs observed in the four datasets.

Parameters	Quantity	Fe I 6302 $\AA$ wideband	Fe I 6302 $\AA$ line core	Fe I 6173 $\AA$ wideband	Ca II H
Size $[km^2]$ [a]	Mean	33,711	37,700	33,530	37,719
	Maximum	38,193	38,193	38,193	38,193
	Minimum	2,288	27,085	2,419	25,386
	σ [b]	3,552	958	4,240	930
Total Intensity [I/$< I_{QS} >$] [c]	Mean	16	21	16	24
	Maximum	24	28	25	47
	Minimum	1	13	1	11
	σ	2.3	1.8	2.6	4.8
Mean Intensity [I/$< I_{QS} >$]	Mean	1.3	1.5	1.3	1.7
	Maximum	1.7	1.9	1.7	3.6
	Minimum	1.1	1.1	1	0.9
	σ	0.1	0.1	0.1	0.3
Maximum Intensity [I/$< I_{QS} >$]	Mean	1.3	1.5	1.3	1.8
	Maximum	1.8	2.0	1.8	3.7
	Minimum	1.0	1.1	1.0	0.9
	σ	0.1	0.1	0.1	0.3
Lifetime $[s]$	Mean	85	45	84	49
	Maximum	1092	812	1372	616
	Minimum	28.00	28.00	14.00	28.00
	σ	102	45	104	52
Horizontal Velocity $[km/s]$	Mean	1.61	1.64	2.80	1.66
	Maximum	3.16	3.16	6.31	3.16
	Minimum	0.	0.	0.	0.
	σ	0.8	0.8	1.4	0.8
Number oF MBPs	Detected	22,195	26,782	53,039	18,372
	Tracked	13,969	11,522	38,694	8,788

[a] This is the size of all detected MBP.

[b] Standard deviations of the distributions

[c] The three regims of intensity are computed relative to the $< I_{QS} >$ average image intensity of each frame in the corresponded dataset.

Note: the results in this Table for size and three intensities are acquired by the detecting algorithm. The lifetime and horizontal velocity are computed by the tracking code.

standard deviation for the total intensity which are 2.3, 1.8, 2.6, and 4.8$< I_{QS} >$ for Fe I 6302 $\mathring{A}$ wideband, Fe I 6302 $\mathring{A}$ line core, Fe I 6173 $\mathring{A}$ wideband, and Ca II H, respectively. Figures 5.1 and 5.2 show the distributions of normalized Mean and total intensity (normalized to average image intensity) for all the four datasets. Each dashed line shows the corresponding mean value which the lines for Fe I 6302 $\mathring{A}$ wideband and Fe I 6173 $\mathring{A}$ wideband are overlapped.

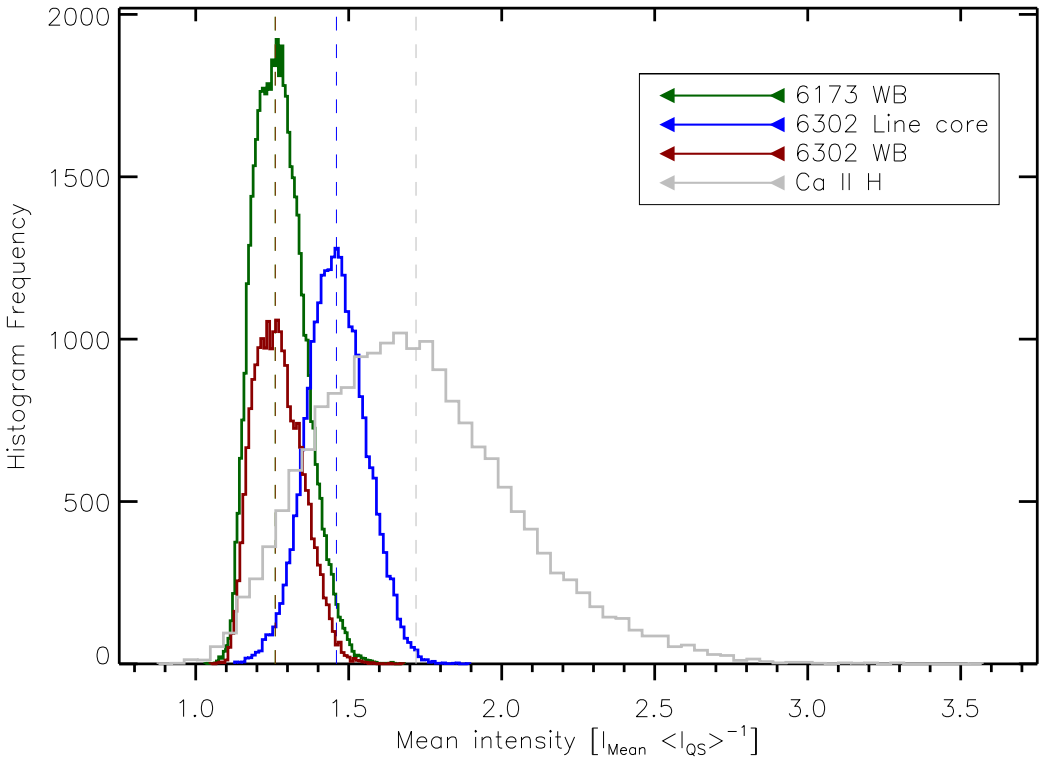

Figure 5.1: Distributions of mean intensity of all identified MBPs in four datasets Fe I 6173 $\mathring{A}$ wideband, Fe I 6302 $\mathring{A}$ wideband, Fe I 6302 line core, and Ca II H are overplotted. The annotation legend box shows the accordant colors for each passband, also the dash line show the mean values.

5.1.2 Size

The size of MBPs that we obtained here, is computed based on the FWHM of the intensity profile and measured in the unit of km^2. The Figure 5.3 displays distributions of the size of all the deleted MBPs in the four datasets.
The observed MBPs in the Fe I 6302 $\mathring{A}$ wideband and Fe I 6173 $\mathring{A}$ wideband have shown to have the smallest minimum areas with 2,288 km^2 and 2,419 km^2, respectively (i.e, they are equivalent to diameters of 54 and 55 km as well.), in this study. Also, Their measured

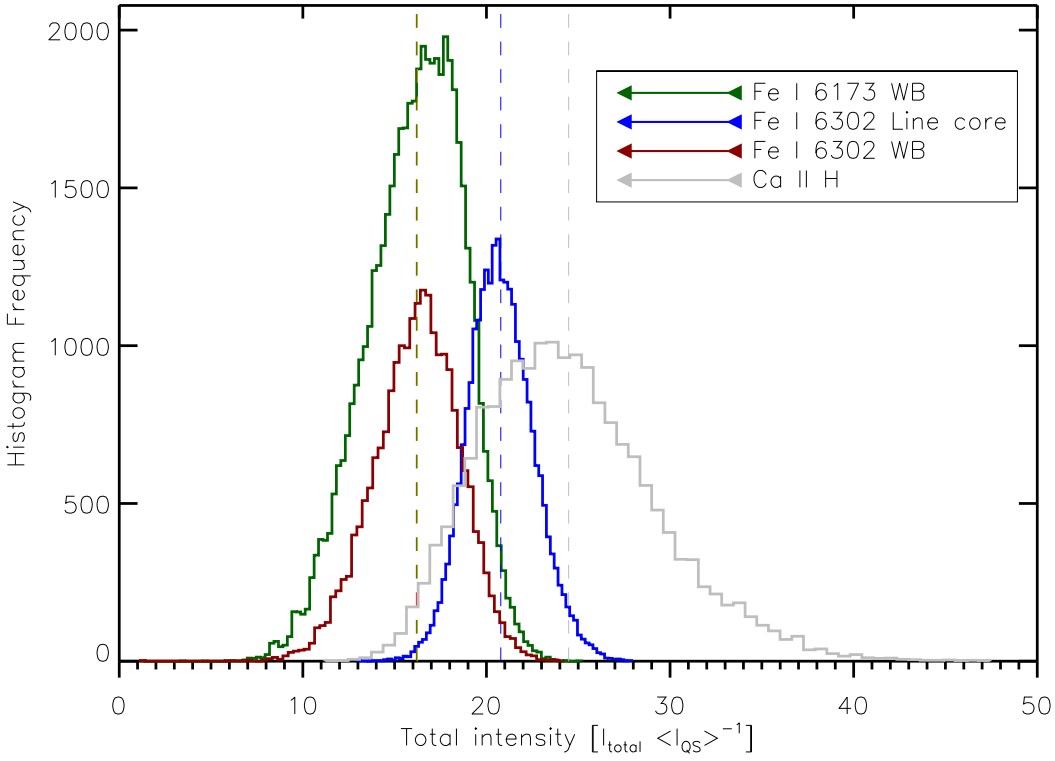

Figure 5.2: Distributions of total intensity of MBPs for four datasets.

mean size are approximately in the same range and smaller than mean size of MBPs that were observed through Fe I 6302 $\mathring{A}$ line core and Ca II H passband filters (i.e., their mean sizes are identical as well.). The results from Fe I 6302 $\mathring{A}$ line core declares the minimum of the measured size for MBPs in this dataset, is the largest minimum value 27,085 km^2. This is equivalent to 1.43 arcsec^2. We noted that the standard deviation of our measurements for the area of MBPs detected in the Fe I 6302 $\mathring{A}$ wideband, Fe I 6173 $\mathring{A}$ wideband, 6302 $\mathring{A}$ line core, and Ca II H are 3,552, 4,240, 958, 930 km^2, respectively. The maximum size of MBPs for all datasets has been found similar in this method and is computed 38,193 km^2 or 19.5 pixel^2.

Distributions of diameter of the MBPs determined using the tracked algorithm are shown in Figure 5.4. This measurement is for the dynamic MBPs which are tracked and we explained as the second approach for measuring the size in 4.1.4. Therefore, the number and size of detected MBPs are not measured identically in the two methods as well as two latter plots. In the two plots, the mean value of each dataset is shown with a dashed line.

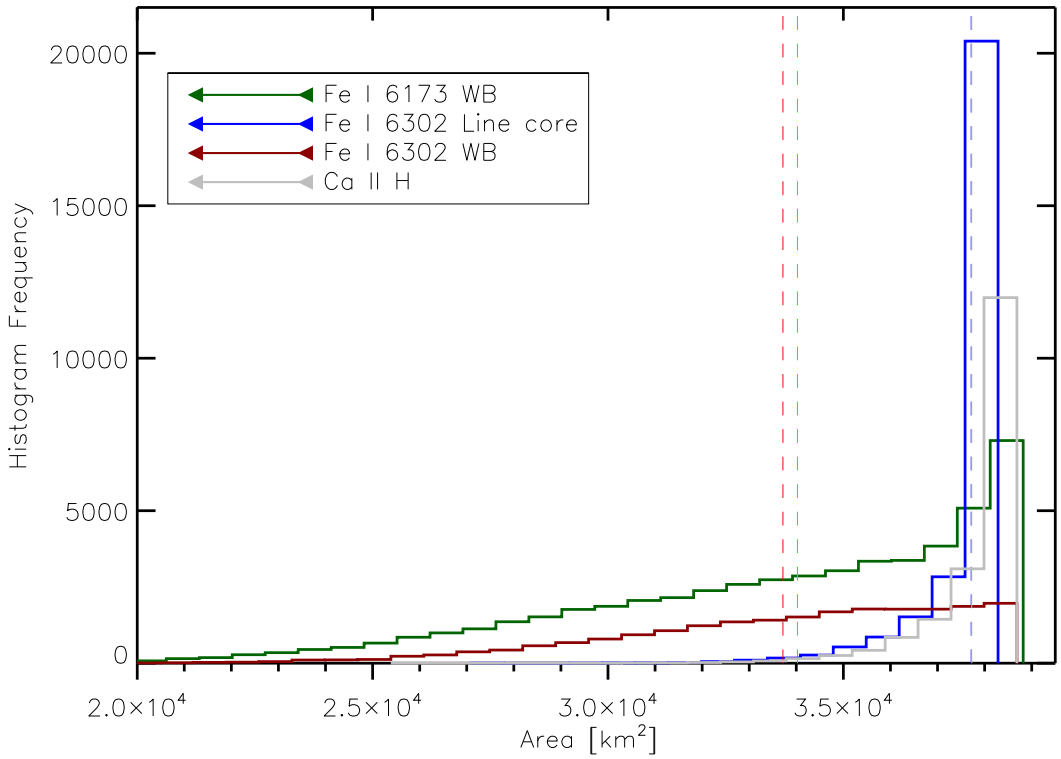

Figure 5.3: The area distributions for all MBPs which are defined based on the FWHM of the intensity profile. The mean size of MBPs in each dataset is indicated with a dashed line. The blue and gray lines corresponded to Fe I 6302 $\mathring{A}$ line core and Ca II H, respectively are approximately overlapped.

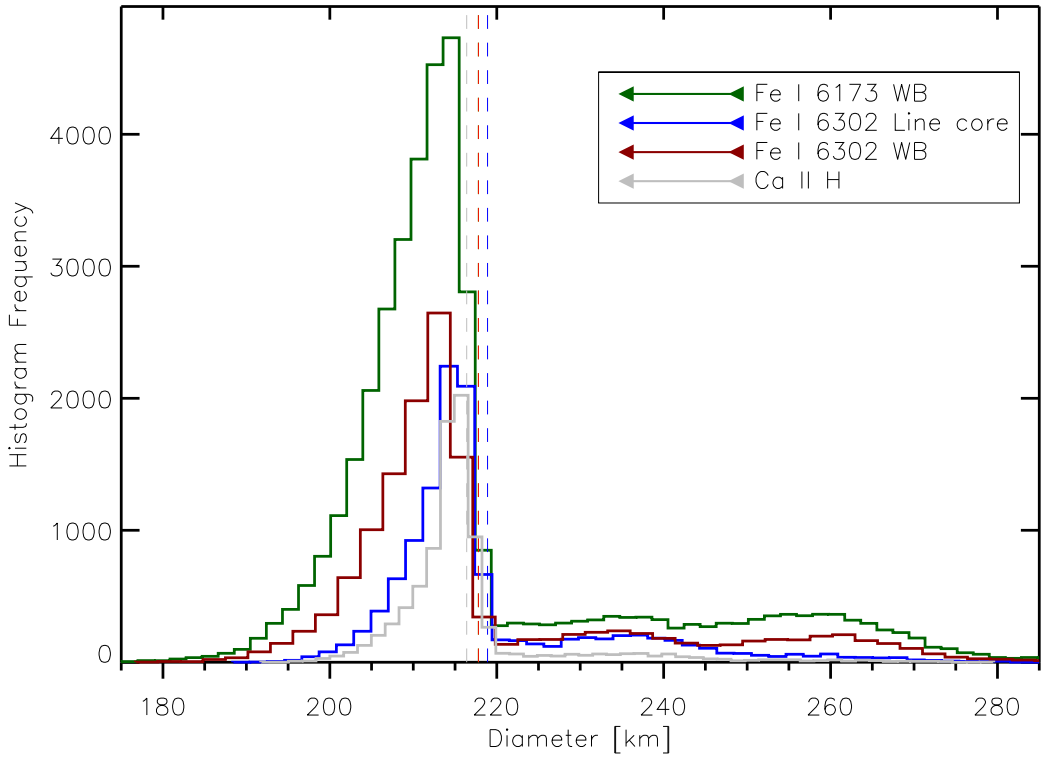

Figure 5.4: Distributions of diameter of all MBPs which are measured using our tracking algorithm. The mean size of MBPs in each dataset is shown with a dashed line. The green and red lines are overlapped.

5.2 Dynamical Parameters Analysis

5.2.1 lifetime

The summarized information in Table 5.1 shows the range of MBPs lifetime with the mean values. The longest lived MBPs were observed in the Fe I 6173 $\mathring{A}$ wideband images with a lifetime of 1,372 seconds. The minimum lifetime allocates to those MBPs which exist in one frame. Hence, they represent the cadence of observations.

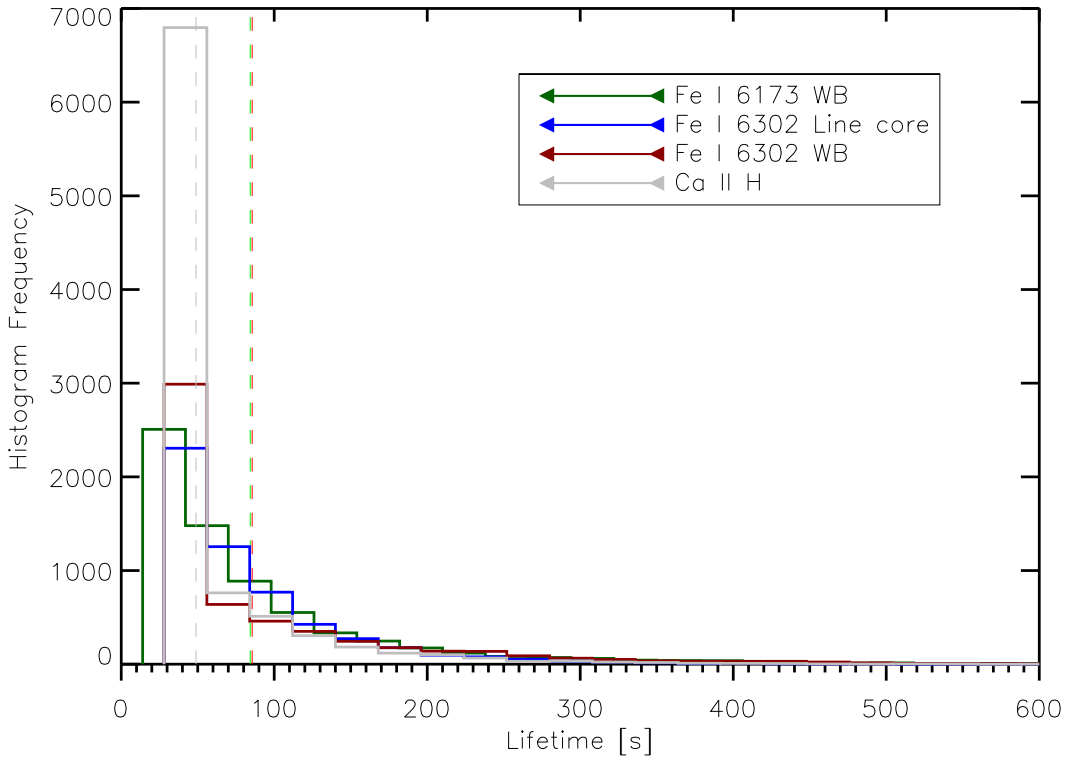

Figure 5.5: Distributions of lifetime for the tracked MBPs. The dashed lines indicate their mean values.

The MBPs in the Fe I 6302 $\mathring{A}$ wideband last in 3 frames on average which it almost equals to the average lifetime of MBPs observed in the Fe I 6302 $\mathring{A}$ wideband, is measured 84 seconds. While, they live in 6 frames due to their shorter cadence. The maximum lifetime is measured 1,092 seconds for the observed MBPs in the Fe I 6302 $\mathring{A}$ wideband. The obtained results for MBPs in Fe I 6302 $\mathring{A}$ line core and Ca II H show their mean lifetime are 45 and 49 seconds, respectively. Amongst the all identified MBPs in this research, we found also that the shortest maximum lifetime is corresponded to the tracked MBPs in the Ca II H passband (616 seconds). While, the measured lifetime of MBPs detected in Fe I 6302 $\mathring{A}$ line core shows that they lived in 29 frames in maximum. Figure 5.5 displays the

over plotted histograms of the lifetime for all datasets.

5.2.2 Horizontal velocity

The obtained results from the three datasets Fe I 6302 $\mathring{A}$ wideband, Fe I 6302 $\mathring{A}$ line core, and Ca II H indicate MBPs move with on approximately similar range of speeds in the horizontal plane, between 0 and 3.16 km/s. This range is substantially different from those observed in the Fe I 6173 $\mathring{A}$ wideband in which the MBPs move with a horizontal velocity between 2.8 and 6.3 km/s. The computed standard deviation for this set of observation is 1.4 km/s, while it is similar for the measurement of horizontal velocity for MBPs observed in those three passbands, acquired 0.8 km/s.
The distribution of horizontal velocity for the MBPs observed in the four datasets are over plotted in figure.5.6.

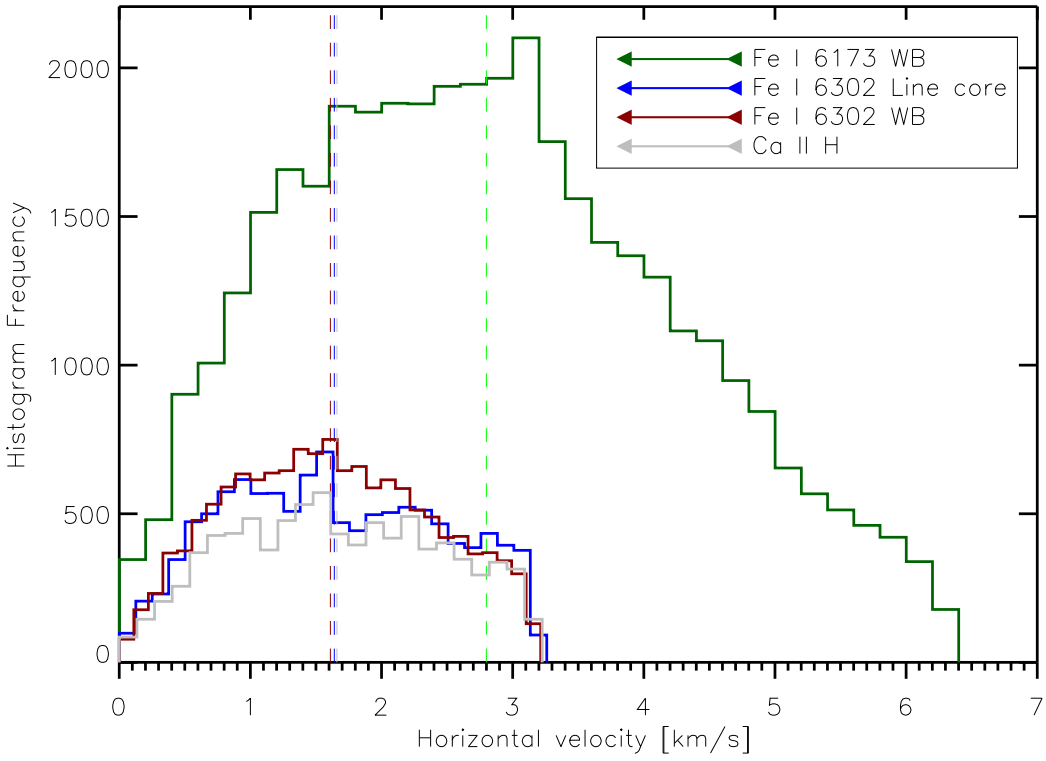

Figure 5.6: Histograms of MBPs' horizontal velocity for four datasets. The dashed lines show the corresponded average horizontal velocities.

5.3 Correlations

We inspect whether the rise and fall of one parameter can have an influence on the increase or decrease of the others. Therefore, it is appropriate to find the correlation between the measured parameters. Here, we represent and discuss the study of correlation between the size and intensity, and the relationship between the dynamical parameters and physical parameters.

5.3.1 Physical parameters

The correlation between the size of MBPs and their intensity is examined. The examination is considered between size and Maximum and mean intensities. In Figure 5.7 the density plots represent the correlations between MBPs diameter and their maximum intensity which represent a well-fit linear regression line in 95% confidence level with solid red and blue dot-dashed lines. The correlation coefficient for the four datasets is 0.7 on average. We do not find a strong relationship between the size and mean intensity, which a mean correlation coefficient is measured smaller than 0.1.

5.3.2 Correlations of Physical and Dynamical parameters

The dependency among horizontal velocity and size of tracked MBPs is obtained individually. The illustrated plots in Figure 5.8 represent the concentration of each quantity. Here, the plots do not imply any noticeable correlation between the size of MBPs and their horizontal velocity.

The correlation between two dynamical parameters are examined. The lifetime and average horizontal velocity do not show any relation with almost zero correlation coefficient, therefore they vary independently for four datasets. In Figure 5.9 the relationship between the two parameters are displayed.

The lifetime of tracked MBPs is compared with their size to inspect if they show any dependency. This comparison is shown in Figure 5.10. The size of MBPs is specified with their diameters and obtained in tracking phase. The measured correlation coefficient, less than 0.1 shows a weak correlation for these two parameters. Therefore, the average horizontal velocity of each tracked MBP should not affect its lifetime or reversely.
The inspection for the relationship between the maximum intensity and maximum horizontal velocity of MBPs indicates very weak correlation between them, with a correlation coefficient of smaller than 0.1. Their density plots for different observations are represented in Figure 5.11. The solid red line and blue dot-dashed line shows the fit of linear regression in 95% confidence level.

Final comparison is inspected between the lifetime of the tracked MBPs and their maximum intensity during their lifetime in the corresponding datasets. As in Figure 5.12 is shown, a relatively weak correlation is seen between them with a correlation coefficient around 0.3.

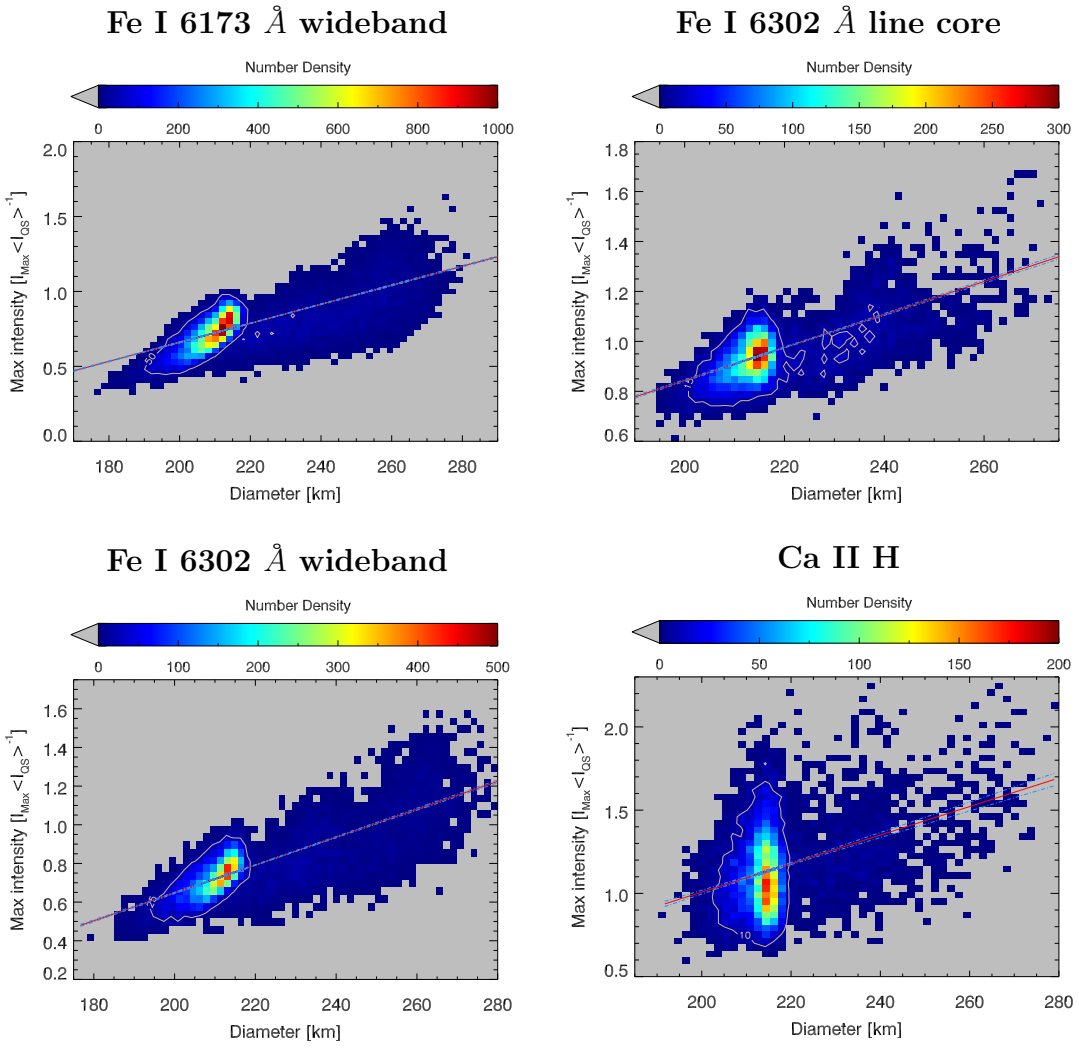

Figure 5.7: The density plots of size and peak intensity of MBPs in the four different datasets.

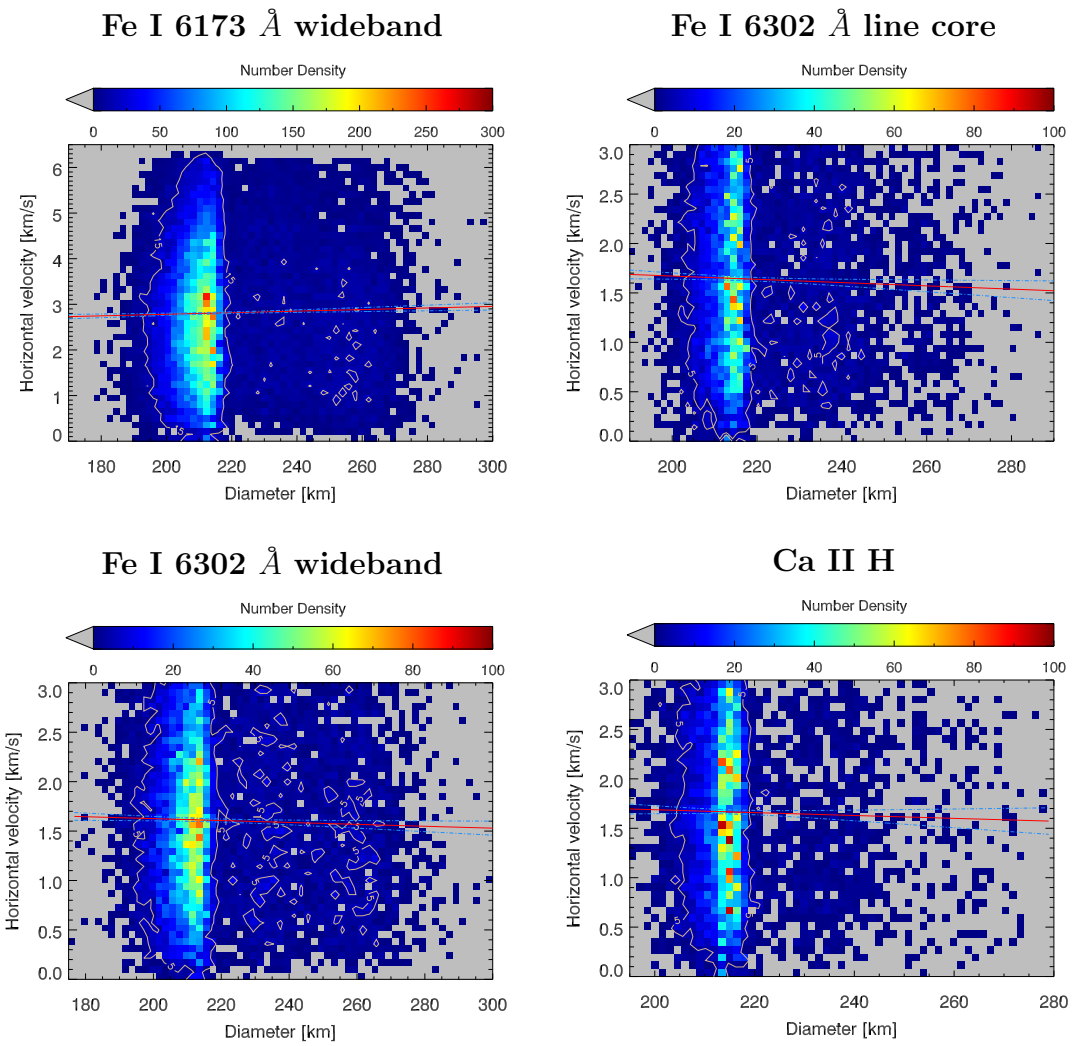

Figure 5.8: Four density plots of the MBPs' diameter and their horizontal velocity in the four different datasets.

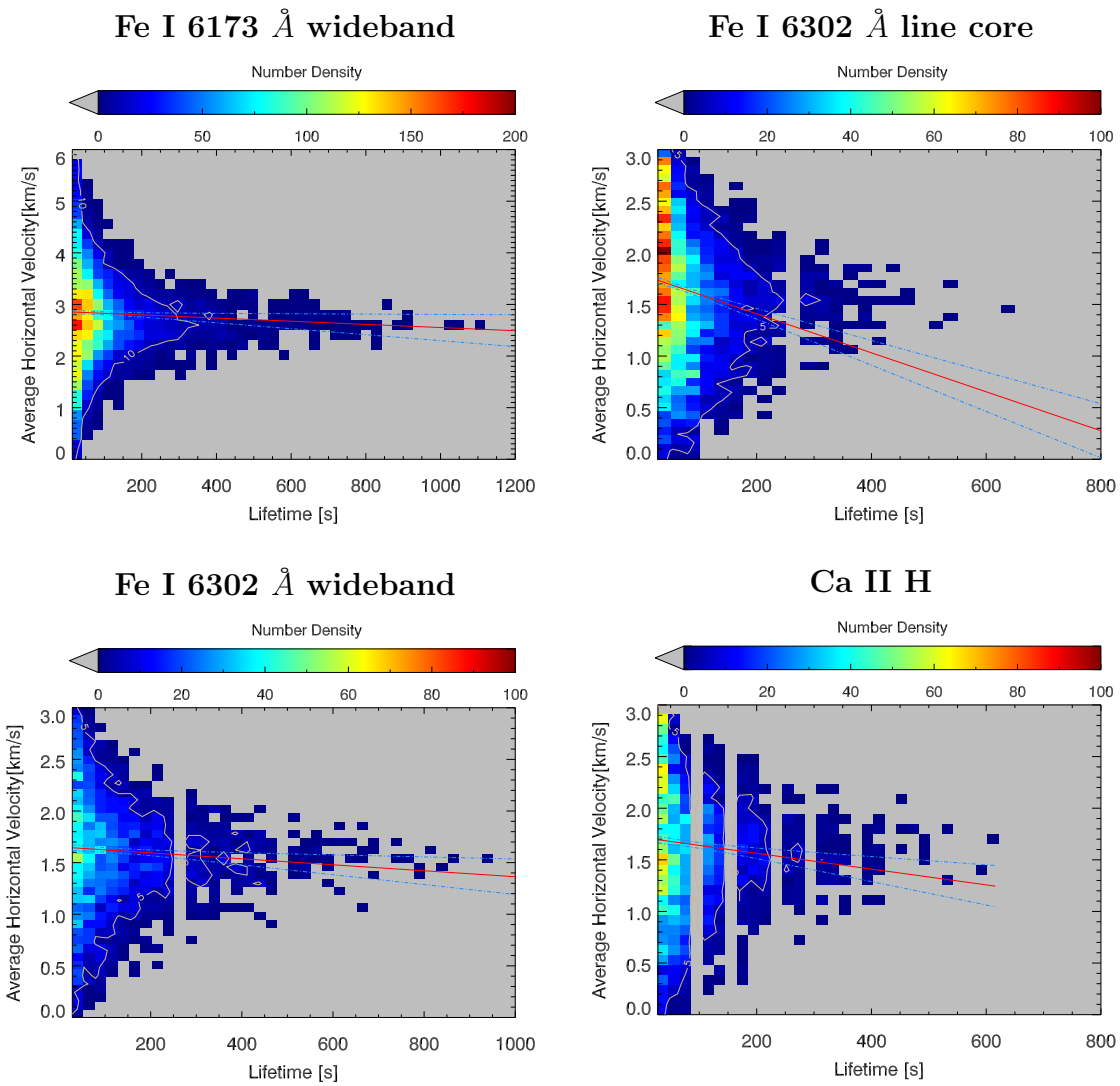

Figure 5.9: The density plots of the lifetime and average horizontal velocity for the four datasets.

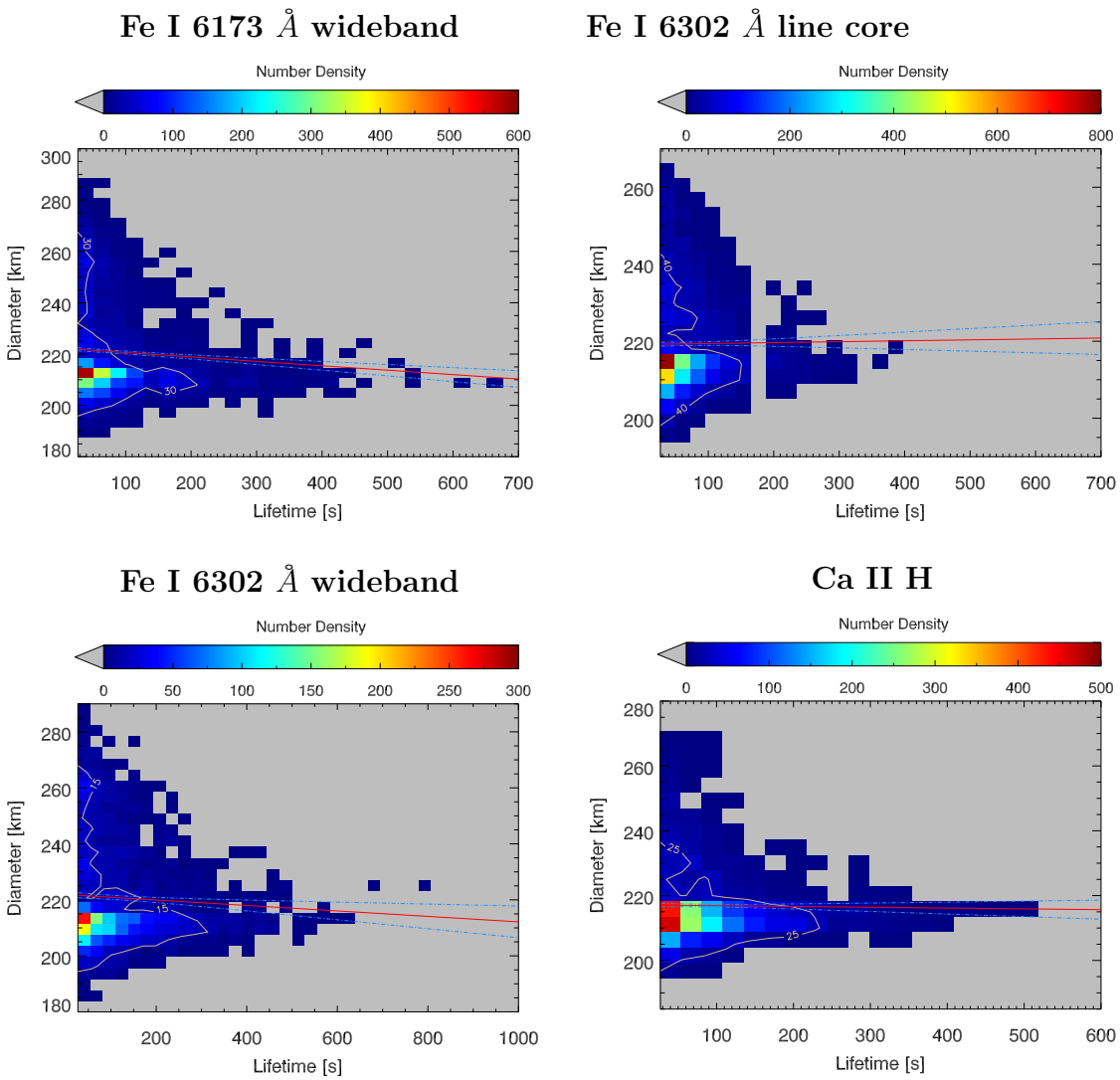

Figure 5.10: The sizes of MBPs (in diameter) and their lifetimes are plotted for four different datasets.

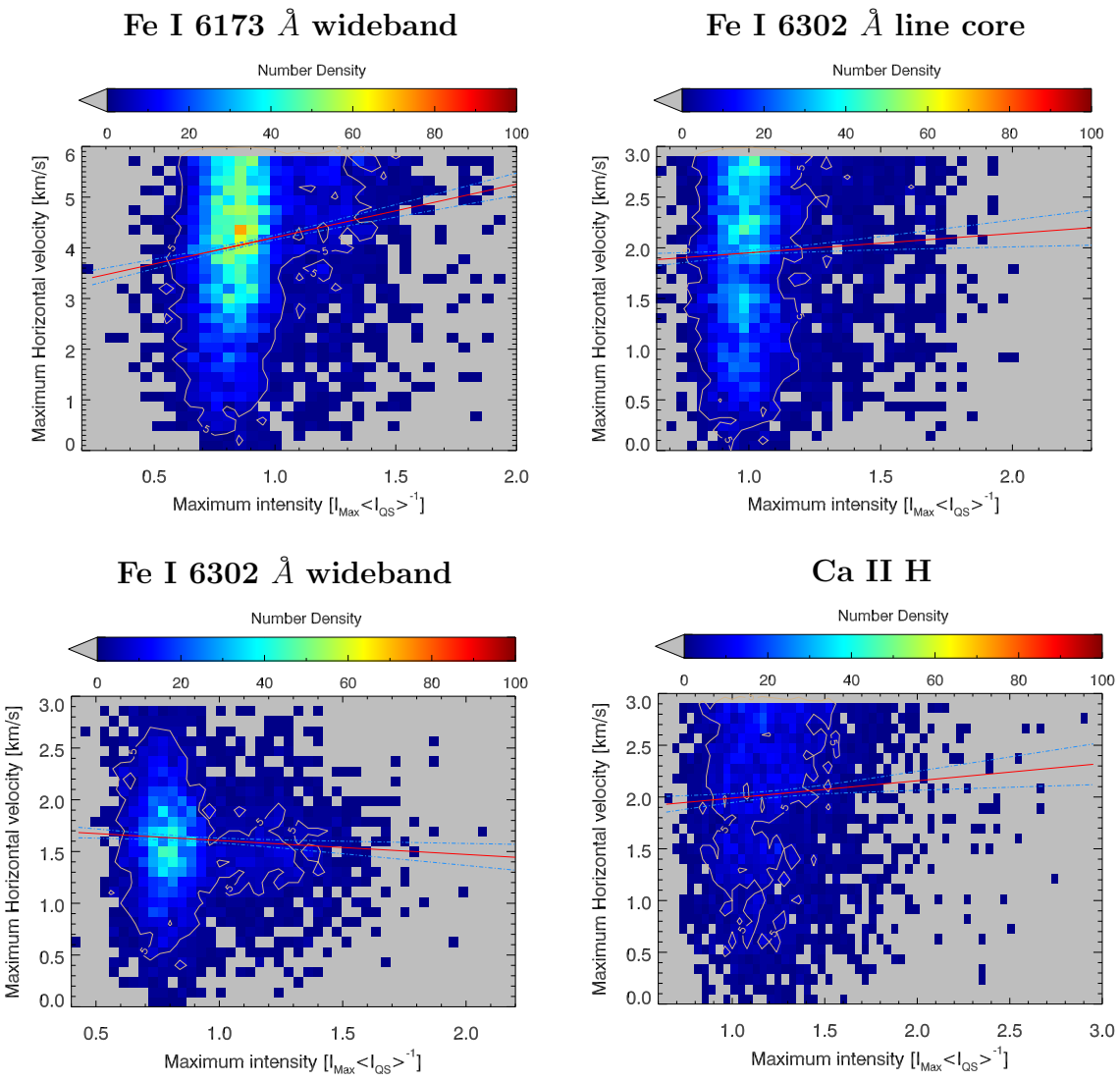

Figure 5.11: Maximum intensity versus maximum horizontal velocity of MBPs for four datasets.

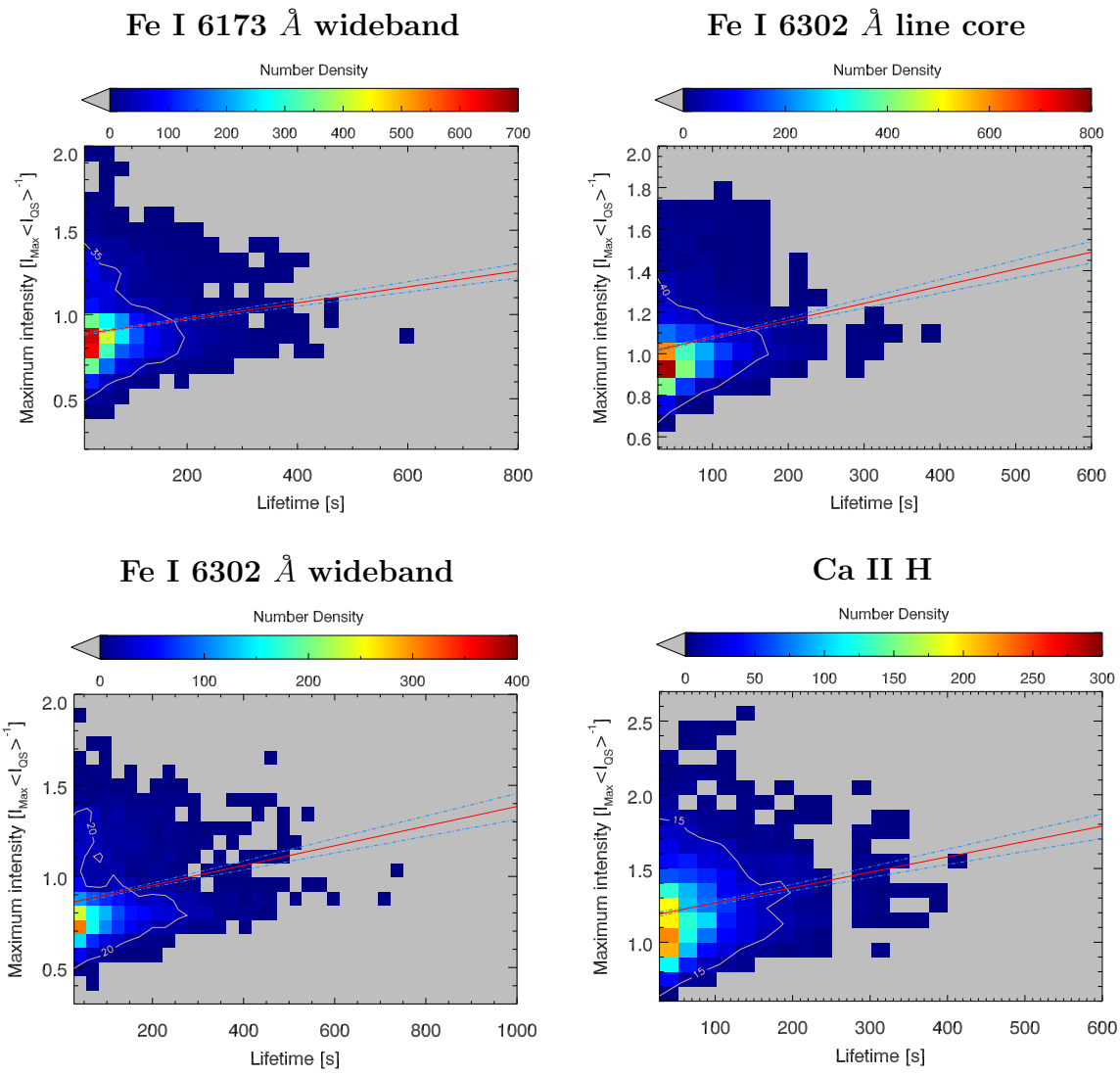

Figure 5.12: Peak of maximum intensity versus Lifetime of MBPs for the four datasets.

Chapter 6

Discussion and Conclusions

In this thesis, we have obtained observational properties of small-scale magnetic bright points (MBPs; associated with strong magnetic elements) in the quiet-sun disc center. We analyzed the MBPs in observations made in Fe I 6302 $\mathring{A}$ wideband, Fe I 6302 $\mathring{A}$ line core, Fe I 6173 $\mathring{A}$ wideband, and Ca II H passband, sampling three different heights in the solar atmosphere, recorded with the Swedish Solar Telescope (SST).

The MBPs were detected by employing a semi-automated algorithm. In this method, the selection of candidate bright features were performed manually, followed by an automated detecting algorithm underlying a set of iterative solutions. Consequently, two physical parameters acquired to describe the area and intensity of identified MBPs as well as their locations.

The selection was restricted by considering four criteria with which the MBPs were defined: (1) were isolated and did not interact with other bright features, (2) were located in intergranular area, (3) were associated with strong Stokes V signals, and (4) were approximately roundish shaped features and were not significantly stretched. Therefore, a number of MBPs that were not satisfying these criteria excluded from our samples.

We defined two approaches that were used in this work to define the size of MBPs. One which was provided in the detecting code obtained based on the FWHM of the intensity profile. The other definition is based on obtaining diameter of MBPs by computing rms of intensity-weighted distances inside a MBP from its center of gravity of density.
In order to clarify the dynamic properties such as lifetime and horizontal velocity, the detected MBPs were tracked using an automated algorithm by linking their positions, and hence, the dynamic properties of tracked MBPs were measured.

The average heights of formation of the datasets used in this investigation are 60, 120, 820 km for Fe I 6302 $\mathring{A}$ wideband/Fe I 6173 $\mathring{A}$ wideband (i.e., the same height), Fe I 6302 $\mathring{A}$ line core, and Ca II H passbands, respectively. These were the results of a computation with the 1D RH-code in non-LTE and the FALP model atmosphere. The FALP model atmosphere has shown to some extent [21] represent the formation height of MBPs.Thus, on average, the MBPs observed in Fe I 6302 $\mathring{A}$ wideband/Fe I 6173 $\mathring{A}$ wideband are in the lower photosphere, Fe I 6302 $\mathring{A}$ line core may show the MBPs in the upper photosphere,

and finally Ca II H dataset represents those in the low chromospheric layers.

In total, we observed 120,388 MBPs during a total time of 10,766 s in 476 frames from all datasets, and tracked 72,973 dynamic MBPs in three heights of the lower solar atmosphere. We found that the MBPs in the two datasets sampling the lower photosphere (i.e., Fe I 6302 $\mathring{A}$ wideband/Fe I 6173 $\mathring{A}$ wideband) have similar physical and dynamical parameters, except that for horizontal velocity. The MBPs observed in this height are approximately the smallest MBPs in this study with a mean diameter equal 105 km, whereas diameter of the MBPs have a mean value of 112 km from observations in Ca II H and Fe I 6302 $\mathring{A}$ line core.

We found that the MBPs in the higher atmospheric heights, sampled by Ca II H and Fe I 6302 $\mathring{A}$ line core, to be on average brighter compared to those studied in the two wideband datasets. The brightness of the MBPs were found to be larger than, or equal to, the brightness of average image intensity for all datasets, except for those in the Ca II H images. The mean value for the latter was found to be $0.9 < I_{QS} >$.
The MBPs corresponding to the lower photosphere, live longer on average (with a mean lifetime of 85 s) compared to those detected in the lower chromosphere and the upper photosphere with mean lifetime of 45 s and 49 s, respectively. The distribution of horizontal velocity of MBPs in Fe I 6173 $\mathring{A}$ wideband demonstrated that they move, on average, with twice speed as the other datasets.

As stated in section 2.4, MBPs are the cross-section of flux tubes which reside in intergranular lanes. Therefore, granular and intergranular motions [19] can influence horizontal motion of MBPs. Hence, the fast motion of MBPs sometimes supersonic, could be related to fast granular flows at the intergranular regions ([21], [3]). Therefore, the fast horizontal velocity of MBPs in the Fe I 6173 $\mathring{A}$ wideband may be interpreted with the latter fact. This is , however, not clear why the MBPs we studied in the other datasets, and in particular, those in Fe I 6302 $\mathring{A}$ wideband do not show similar velocities. This is interesting since the latter MBPs are thought to be approximately located in the same atmospheric height as those observed in Fe I 6173 $\mathring{A}$ wideband images.

Furthermore, we studied the correlations amongst different parameters. This investigation clarified that the area of MBPs and their intensity have a noticeable correlations i.e., the total and maximum intensities with the area of MBPs. The mean intensity of the MBPs showed a weak correlation with the area. Hence, we may interpret that the larger MBPs are brighter in all the three different heights, studied here. We also found a direct relationship between lifetimes and maximum intensities of the MBPs in all datasets. We did not find correlations among other parameters. In particular, no clear relationship was seen between maximum velocities and peak intensities of the MBPs. As it had been reported by [21] for Ca II H MBPs. The latter was, however, limited to the smallest features in internetwork areas.

Further detail inspections based on, e.g., size of MBPs, from observations and MHD simulations (in various atmospheric height) might clarify these controversies.

Bibliography

[1] V. Abramenko, V. Yurchyshyn, and P. R. Goode. Size and Life Time Distributions of Bright Points in the Quiet Sun Photosphere. *AGU Fall Meeting Abstracts*, page C1806, December 2010.

[2] E. H. Avrett and R. Loeser. Models of the Solar Chromosphere and Transition Region from SUMER and HRTS Observations: Formation of the Extreme-Ultraviolet Spectrum of Hydrogen, Carbon, and Oxygen. *Astrophysical Journal, Supplement*, 175:229–276, March 2008.

[3] L. R. Bellot Rubio. Detection of Supersonic Horizontal Flows in the Solar Granulation. *Astrophysical Journal*, 700:284–291, July 2009.

[4] T. E. Berger, M. G. Löfdahl, R. S. Shine, and A. M. Title. Measurements of Solar Magnetic Element Motion from High-Resolution Filtergrams. *Astrophysical Journal*, 495:973–983, March 1998.

[5] B. Caccin, M. T. Gomez, C. Marmolino, and G. Severino. Response functions and contribution functions of photospheric lines. *Astronomy and Astrophysics*, 54:227–231, January 1977.

[6] M. Carlsson and R. Stein. CA II K2V Bright Grains Formed by Acoustic Waves. In M. S. Giampapa and J. A. Bookbinder, editors, *Cool Stars, Stellar Systems, and the Sun*, volume 26 of *Astronomical Society of the Pacific Conference Series*, page 515, 1992.

[7] M. Carlsson and R. F. Stein. Formation of Solar Calcium H and K Bright Grains. *Astrophysical Journal*, 481:500–514, May 1997.

[8] G. A. Chapman. On the Nature of the Small-Scale Solar Magnetic Field. *Astrophysical Journal*, 191:255–260, July 1974.

[9] A. R. Choudhuri, M. Dikpati, and D. Banerjee. Energy transport to the solar corona by magnetic kink waves. *Astrophysical Journal*, 413:811–825, August 1993.

[10] J. C Crocker and D. G Grier. Methods of digital video microscopy for colloidal studies. *Journal of colloid and interface science*, 179(1):298–310, 1996.

[11] J. de la Cruz Rodriguez, M. G. Löfdahl, P. Sütterlin, T. Hillberg, and L van der Voort Rouppe. CRISPRED: A data pipeline for the CRISP imaging spectropolarimeter. *Astronomy & Astrophysics*, 573:A40, January 2015.

[12] R. B. Dunn and J. B. Zirker. The Solar Filigree. *Solar Physics*, 33:281–304, December 1973.

[13] T. L. Duvall, Jr. Large-scale solar velocity fields. *Solar Physics*, 63:3–15, August 1979.

[14] J. M. Fontenla, E. Avrett, G. Thuillier, and J. Harder. Semiempirical Models of the Solar Atmosphere. I. The Quiet- and Active Sun Photosphere at Moderate Resolution. *Astronomy and Astrophysics*, 639:441–458, March 2006.

[15] J. M. Fontenla, E. H. Avrett, and R. Loeser. Energy balance in the solar transition region. III - Helium emission in hydrostatic, constant-abundance models with diffusion. *Astronomy and Astrophysics*, 406:319–345, March 1993.

[16] U. Grossmann-Doerth, M. Schuessler, and O. Steiner. Convective intensification of solar surface magnetic fields: results of numerical experiments. *Astronomy and Astrophysics*, 337:928–939, September 1998.

[17] G. E. Hale. On the Probable Existence of a Magnetic Field in Sun-Spots. *Astrophysical Journal*, 28:315, November 1908.

[18] V. M. J. Henriques. *Three-dimensional mapping of fine structure in the solar atmosphere*. PhD thesis, University of Stockholm, 2013.

[19] J. Hirzberger, J. A. Bonet, M. Vázquez, and A. Hanslmeier. Time Series of Solar Granulation Images. II. Evolution of Individual Granules. *Astrophysical Journal*, 515:441–454, April 1999.

[20] S. Jafarzadeh, L. Rouppe van der Voort, and J. de la Cruz Rodríguez. Magnetic Upflow Events in the Quiet-Sun Photosphere. I. Observations. *Astrophysical Journal*, 810:54, September 2015.

[21] S. Jafarzadeh, S. K. Solanki, A. Feller, A. Lagg, A. Pietarila, S. Danilovic, T. L. Riethmüller, and V. Martínez Pillet. Structure and dynamics of isolated internetwork Ca II H bright points observed by SUNRISE. *Astronomy and Astrophysics*, 549:A116, January 2013.

[22] D. B. Jess, D. J. Pascoe, D. J. Christian, M. Mathioudakis, P. H. Keys, and F. P. Keenan. The Origin of Type I Spicule Oscillations. *Astrophysical Journal, Letters*, 744:L5, January 2012.

[23] D. B. Jess, S. Shelyag, M. Mathioudakis, P. H. Keys, D. J. Christian, and F. P. Keenan. Propagating Wave Phenomena Detected in Observations and Simulations of the Lower Solar Atmosphere. *Astrophysical Journal*, 746:183, February 2012.

[24] P. H. Keys, M. Mathioudakis, D. B. Jess, D. H. Mackay, and F. P. Keenan. Dynamic properties of bright points in an active region. *Astronomy and Astrophysics*, 566:A99, June 2014.

[25] P. H. Keys, M. Mathioudakis, D. B. Jess, S. Shelyag, D. J. Christian, and F. P. Keenan. Tracking magnetic bright point motions through the solar atmosphere. *Monthly Notices of the RAS*, 428:3220–3226, February 2013.

[26] P. H. Keys, M. Mathioudakis, D. B. Jess, S. Shelyag, P. J. Crockett, D. J. Christian, and F. P. Keenan. The Velocity Distribution of Solar Photospheric Magnetic Bright Points. *Astrophysical Journal, Letters*, 740:L40, October 2011.

[27] K. Langhans, W. Schmidt, and A. Tritschler. 2D-spectroscopic observations of vec G-band bright structures in the solar photosphere. *Astronomy and Astrophysics*, 394:1069–1076, November 2002.

[28] M. G. Löfdahl. *Phase diversity wavefront sensing and image restoration applied to high-resolution solar observations.* PhD thesis, Royal Swedish Academy of Sciences Stockholm Observatory SE-133 36 Saltsjöbaden Sweden ¡EMAIL¿mats@astro.su.se¡/EMAIL¿, 1996.

[29] M. G. Löfdahl. Multi-frame blind deconvolution with linear equality constraints. In P. J. Bones, M. A. Fiddy, and R. P. Millane, editors, *Image Reconstruction from Incomplete Data*, volume 4792 of *Society of Photo-Optical Instrumentation Engineers (SPIE) Conference Series*, pages 146–155, December 2002.

[30] M. G. Löfdahl and G. B. Scharmer. Sources of straylight in the post-focus imaging instrumentation of the Swedish 1-m Solar Telescope. *Astronomy and Astrophysics*, 537:A80, January 2012.

[31] J. P. Mehltretter. Observations of photospheric faculae at the center of the solar disk. *Solar Physics*, 38:43–57, September 1974.

[32] N. Meunier, T. Roudier, and M. Rieutord. Supergranules over the solar cycle. *Astronomy and Astrophysics*, 488:1109–1115, September 2008.

[33] E. N. Parker. Topological Dissipation and the Small-Scale Fields in Turbulent Gases. *Astrophysical Journal*, 174:499, June 1972.

[34] E. N. Parker. Magnetic Neutral Sheets in Evolving Fields - Part Two - Formation of the Solar Corona. *Astrophysical Journal*, 264:642, January 1983.

[35] E. N. Parker. Nanoflares and the solar X-ray corona. *Astrophysical Journal*, 330:474–479, July 1988.

[36] E. N. Parker. Solar Magnetism: The State of Our Knowledge and Ignorance. *Space Science Reviews*, 144:15–24, April 2009.

[37] E. Priest. *Magnetohydrodynamics of the Sun*. May 2014.

[38] M. Rieutord and F. Rincon. The Sun's Supergranulation. *Living Reviews in Solar Physics*, 7:2, June 2010.

[39] R. J. Rutten. Sun-as-a-star line formation. In G. Wallerstein, editor, *Cool Stars, Stellar Systems, and the Sun*, volume 9 of *Astronomical Society of the Pacific Conference Series*, pages 91–102, 1990.

[40] R. J. Rutten, A. G. de Wijn, and P. Sütterlin. DOT tomography of the solar atmosphere. II. Reversed granulation in Ca II H. *Astronomy and Astrophysics*, 416:333–340, March 2004.

[41] J. Sánchez Almeida, I. Márquez, J. A. Bonet, I. Domínguez Cerdeña, and R. Muller. Bright Points in the Internetwork Quiet Sun. *Astrophysical Journal, Letters*, 609:L91–L94, July 2004.

[42] J. Sánchez Almeida, I. Márquez, J. A. Bonet, I. Domínguez Cerdeña, and R. Muller. Bright Points in the Internetwork Quiet Sun. *Astrophisycal Journal*, 609:L91–L94, July 2004.

[43] G. B. Scharmer. Comments on the optimization of high resolution Fabry-Pérot filtergraphs. *Astronomy and Astrophysics*, 447:1111–1120, March 2006.

[44] G. B. Scharmer, K. Bjelksjo, T. K. Korhonen, B. Lindberg, and B. Petterson. The 1-meter swedish solar telescope. In *Astronomical Telescopes and Instrumentation*, pages 341–350. International Society for Optics and Photonics, 2003.

[45] G. B. Scharmer and M. Carlsson. A new approach to multi-level non-LTE radiative transfer problems. *Journal of Computational Physics*, 59:56–80, May 1985.

[46] G. B. Scharmer and M. Carlsson. A new method for solving multi-level non-LTE problems. In J. E. Beckman and L. Crivellari, editors, *NATO Advanced Science Institutes (ASI) Series C*, volume 152 of *NATO Advanced Science Institutes (ASI) Series C*, pages 189–198, 1985.

[47] G. B Scharmer, P. M Dettori, M. G Lofdahl, and M. Shand. Adaptive optics system for the new swedish solar telescope. In *Astronomical Telescopes and Instrumentation*, pages 370–380. International Society for Optics and Photonics, 2003.

[48] G. B. Scharmer, G. Narayan, T. Hillberg, J. de la Cruz Rodríguez, M. G. Löfdahl, D. Kiselman, P. Sütterlin, M. van Noort, and A. Lagg. CRISP Spectropolarimetric Imaging of Penumbral Fine Structure. *Astronomy and Astrophysics*, 689:L69, December 2008.

[49] M. Schüssler. Theoretical Aspects of Small-Scale Photospheric Magnetic Fields. In J. O. Stenflo, editor, *Solar Photosphere: Structure, Convection, and Magnetic Fields*, volume 138 of *IAU Symposium*, page 161, 1990.

[50] S. K. Solanki. Smallscale Solar Magnetic Fields - an Overview. *Space Science Reviews*, 63:1–188, March 1993.

[51] S. K. Solanki, A. Lagg, J. Woch, N. Krupp, and M. Collados. Three-dimensional magnetic field topology in a region of solar coronal heating. *Nature*, 425:692–695, October 2003.

[52] H. C. Spruit. Pressure equilibrium and energy balance of small photospheric fluxtubes. *Solar Physics*, 50:269–295, December 1976.

[53] J. O. Stenflo. Measurements of magnetic fields and the analysis of Stokes profiles. *Solar Physics*, 100:189–208, October 1985.

[54] A. M. Title and T. E. Berger. Double-Gaussian Models of Bright Points or Why Bright Points Are Usually Dark. *Astronomical Journal*, 463:797, June 1996.

[55] A. M. Title, T. D. Tarbell, K. P. Topka, S. H. Ferguson, R. A. Shine, and SOUP Team. Statistical properties of solar granulation derived from the SOUP instrument on Spacelab 2. *Astrophysical Journal*, 336:475–494, January 1989.

[56] H. Uitenbroek. Multilevel Radiative Transfer with Partial Frequency Redistribution. *Astronomy and Astrophysics*, 557:389–398, August 2001.

[57] H. Uitenbroek. The Accuracy of the Center-of-Gravity Method for Measuring Velocity and Magnetic Field Strength in the Solar Photosphere. *Astronomy and Astrophysics*, 592:1225–1233, August 2003.

[58] H. Uitenbroek and C. Briand. The Mg I 285.21 nm Line: an Example of Non-LTE Line Formation. *Astronomy and Astrophysics*, 447:453, July 1995.

[59] D. Utz, A. Hanslmeier, C. Möstl, R. Muller, A. Veronig, and H. Muthsam. The size distribution of magnetic bright points derived from Hinode/SOT observations. *Astronomy and Astrophysics*, 498:289–293, April 2009.

[60] D. Utz, A. Hanslmeier, C. Möstl, R. Muller, A. Veronig, and H. Muthsam. The size distribution of magnetic bright points derived from Hinode/SOT observations. *Astronomy and Astrophysics*, 498:289–293, April 2009.

[61] M. van Noort, L. Rouppe van der Voort, and M. Löfdahl. Solar Image Restoration by use of Multi-Object Multi-Frame Blind Deconvolution. In J. Leibacher, R. F. Stein, and H. Uitenbroek, editors, *Solar MHD Theory and Observations: A High Spatial Resolution Perspective*, volume 354 of *Astronomical Society of the Pacific Conference Series*, page 55, December 2006.

[62] M. van Noort, L. Rouppe van der Voort, and M. G. Löfdahl. Solar Image Restoration By Use Of Multi-frame Blind De-convolution With Multiple Objects And Phase Diversity. *Solar Physics*, 228:191–215, May 2005.

[63] J. E. Vernazza, E. H. Avrett, and R. Loeser. Structure of the solar chromosphere. III - Models of the EUV brightness components of the quiet-sun. *Astrophysical Journal, Supplement*, 45:635–725, April 1981.

[64] J. V. Wall and C. R. Jenkins. *Practical Statistics for Astronomers*. November 2003.

[65] T. Wiegelmann and T. Sakurai. Solar Force-free Magnetic Fields. *Living Reviews in Solar Physics*, 9:5, September 2012.

[66] T. Wiegelmann, J. K. Thalmann, and S. K. Solanki. The magnetic field in the solar atmosphere. *Astronomy and Astrophysics Reviews*, 22:78, November 2014.

[67] M. F. Woodard and J. Chae. Evidence for non-potential magnetic fields in the quiet Sun. *Solar Physics*, 184:239–247, February 1999.

[68] P. Zeeman. On the Influence of Magnetism on the Nature of the Light Emitted by a Substance. *Astrophysical Journal*, 5:332, May 1897.